Parametric Survey of Microfireball Calculations for the Light Ion Fusion Target Development Facility Design

M. Uesaka and G.A. Moses

August 1983

UWFDM-533

FUSION TECHNOLOGY INSTITUTE

UNIVERSITY OF WISCONSIN

MADISON WISCONSIN

Parametric Survey of Microfireball Calculations for the Light Ion Fusion Target Development Facility Design

M. Uesaka and G.A. Moses

Fusion Technology Institute
University of Wisconsin
1500 Engineering Drive
Madison, WI 53706

http://fti.neep.wisc.edu

August 1983

UWFDM-533

PARAMETRIC SURVEY OF MICROFIREBALL CALCULATIONS FOR THE LIGHT ION FUSION TARGET DEVELOPMENT FACILITY DESIGN

M. Uesaka

G.A. Moses

Fusion Engineering Program
Nuclear Engineering Department
University of Wisconsin-Madison
Madison, Wisconsin 53706

August 1983

UWFDM-533

I. Introduction

Light ion beam driven fusion offers the potential of delivering large amounts of energy to an ICF target in the near future [1]. If the focusing of light ions can be brought under control then the PBFA-II facility, currently under construction, is expected to produce scientific breakeven implosions in the mid-1980's. Should this occur on schedule, the following high gain target implosion test facility would become operational in the early 1990's. This facility, called the Light Ion Fusion Target Development Facility (TDF), is currently in the preconceptual design stage [2]. Some proposed parameters for this facility are given in Table 1 and a schematic diagram of it is shown in Fig. 1.

The reaction chamber for this device should be designed to have a lifetime of 15,000 full yield (200 MJ) shots. This lifetime will of course be determined by the fatigue life of the first wall which in turn depends on the stresses generated in the wall. As input to this stress and fatigue analysis one must characterize the overpressure generated at the first wall by the exploding target. This process is shown schematically in Fig. 2. The reaction chamber is filled with a background gas to support the establishment of z-pinch plasma channels for the purposes of ion beam transport from the diodes to the target. For the TDF, nitrogen at a pressure of about 20-30 torr is a good candidate for this gas. The gas attenuates the target generated x-rays and ionic debris, creating a microfireball. This fireball then propagates to the first wall in the form of a radiation diffusion wave and a hydrodynamic shock wave. Thus, to characterize the overpressure at the first wall one must compute the response of the background gas to the target microexplosion.

Table 1. Proposed Parameters for Light Ion Fusion

Target Development Facility

Schedule, Purpose and Characteristics

Schedule	
Preconceptual Design	1981-84
Conceptual Design	1984-86
Engineering Design	1986-88
Construction	1988-93
Operation	1993

Purpose

Test high gain (10-200), high yield (50-800 MJ) ICF targets driven by light ion beams

Qualify high gain targets for eventual reactor applications.

Characteristics	
Lifetime	5 years
Number of Shots	15,000
Shot Rate	10/day
Nominal Yield	200 MJ

Operating Parameters

Target	
Energy Requirement	$\leq$ 4 MJ
Yield	50-800 MJ
Radius	0.5 cm
Driver	
Energy in Store	15 MJ
Energy at Diodes	8 MJ
Diode Voltage	4-30 MW
Power at Diodes	200 TW
Pulse Width at Diodes	40 ns

Plasma Channels	
Length	4. m
Current	85 kA
Number	40-60
Radius at Firing Time	0.5 cm
Cavity Gas	
Type	27 torr Nitrogen
Cavity	
Shape	cylindrical
Height	6 m
Diameter	6 m
Shot Rate	10/day
First Wall	
Material	Al 6061
Thickness	3 cm
Design	Solid plate panels supported by frame
Number of Panels	60
Panel Width	0.47 cm
Panel Height	2 m
Fatigue Life	1.5×10^4
Shield	
Type	Borated water with air bubbles to suppress acoustic waves

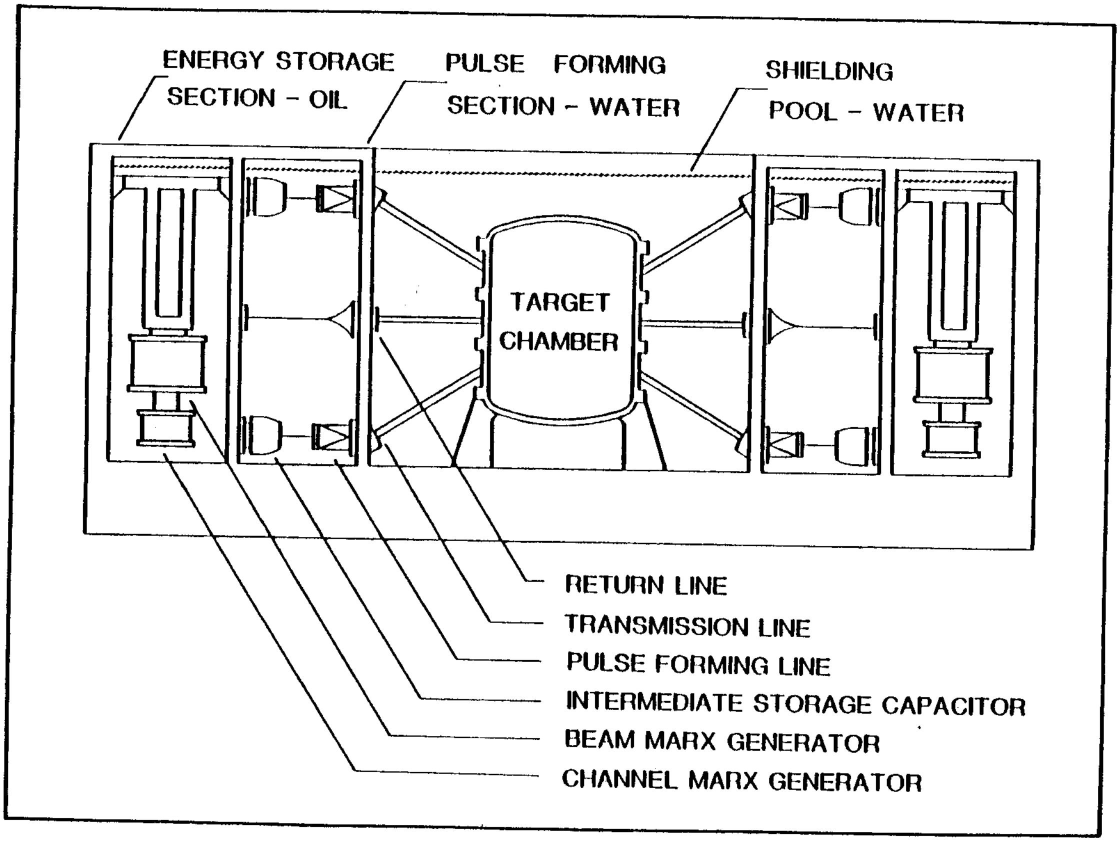

PRECONCEPTUAL LIGHT ION FUSION TARGET DEVELOPMENT FACILITY

Fig. 1. Cross section schematic of light ion fusion target development facility.

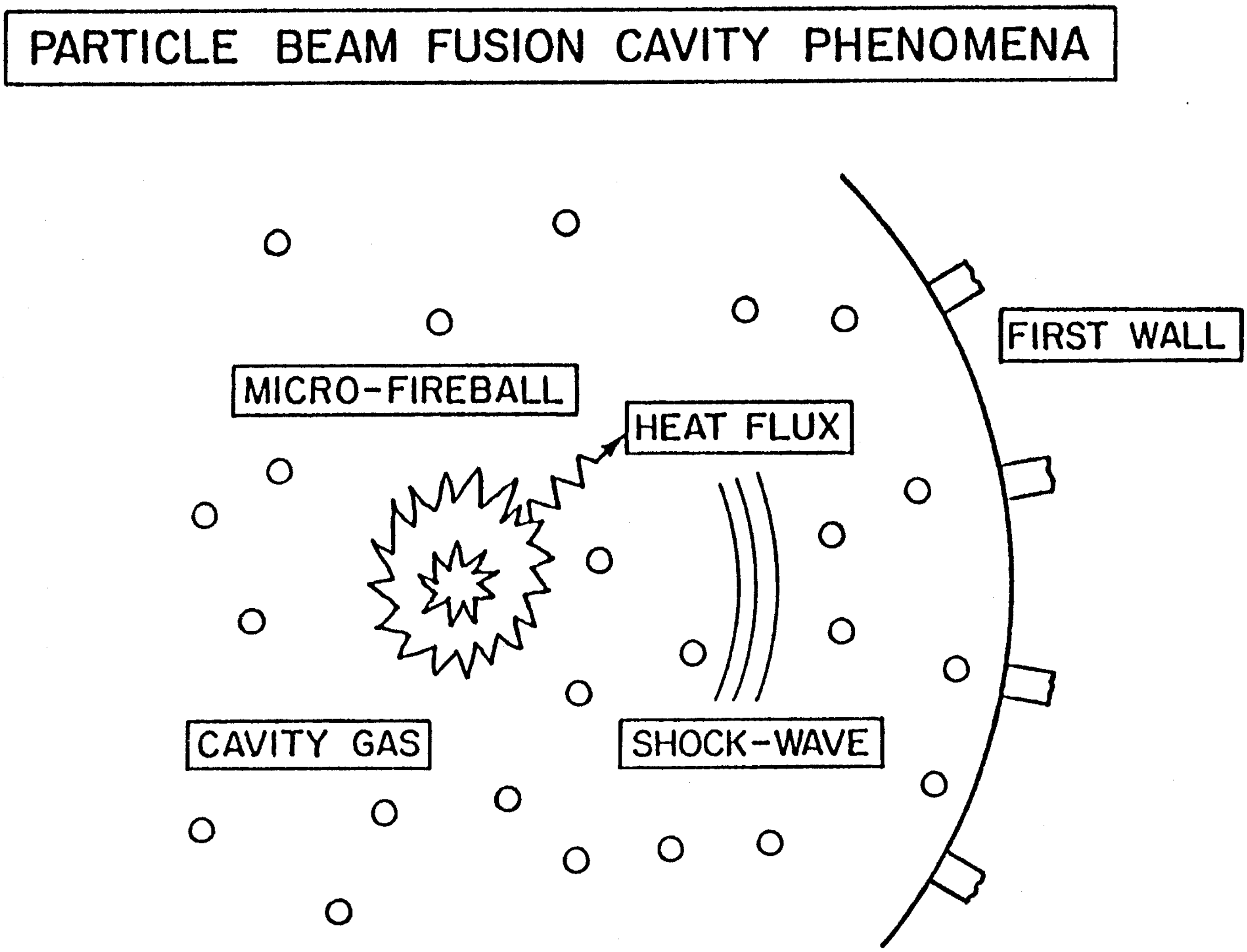

Fig. 2. Schematic picture of target explosion in a gas filled chamber.

Several reports and papers describing microfireball calculations have been published in the past few years [3-5].

In this report, we present a parametric survey of gas response to three significantly different target yields (50 MJ, 200 MJ, and 800 MJ) and three different reaction chamber radii (1.5 m, 3 m, and 6 m). From Table 1 we see that these values bracket the nominal parameters of 200 MJ yield and 6 m diameter chamber. Section II of the report gives a description of the latest radiation-hydrodynamics computer model used for this analysis and Section III contains the results of the calculations and a discussion of their implications. Section IV is devoted to a summary of the work and conclusions. Appendix A contains graphs of the dynamics of all of the calculations used in this survey.

II. Description of the Radiation Hydrodynamics Computer Model

To calculate the dynamics of microfireballs in the TDF cavity, a computer code, MF-FIRE, has been written to simulate the important features of the fireball [6].

The one-fluid hydrodynamic approximation is used and the one-dimensional equation of motion is expressed in Lagrangian coordinates as

$$\frac{\partial u}{\partial t} = -r^{\delta-1} \frac{\partial}{\partial m_0} (P + Q) + \dot{u}_d \tag{1}$$

where m_0 is the Lagrangian mass defined as

$$dm_0 = r^{\delta-1} \rho(r) \; dr \; .$$

The other quantities are the fluid velocity u, the total pressure P, the mass density ρ and one spatial dimension r (δ = 1 planar, δ = 2 cylindrical, δ = 3 spherical). The term, $\dot{u}_d$, is the velocity change in the fluid due to momentum deposition from target debris. The plasma pressure, P_P, is computed from the perfect gas law,

$$P_P = n_P(1 + Z)k_B T_P \tag{2}$$

where Z is the charge state of the plasma, n_p is the number density of plasma atoms and T_p is the plasma temperature. The radiation pressure, P_R, is computed from the radiation energy density, E_R, by

$$P_R = \frac{1}{3} E_R \tag{3}$$

where the radiation energy density has been assumed to be isotropic. The standard shock treatment using the Von Neumann artificial viscosity Q is used [7].

The plasma electrons and ions are assumed to be in equilibrium with each other so that the plasma can be characterized by a single local temperature $T_P(r,t)$. Thermal energy flow through the plasma includes electron thermal conduction and radiation diffusion. Radiation diffusion is treated using the multifrequency group approximation. The coupled plasma and radiation diffusion equations are

$$C_V \frac{\partial T_P}{\partial t} = \frac{\partial}{\partial m_o} \left(r^{\delta-1} k_P \frac{\partial T_P}{\partial r}\right) - \frac{\partial P_P}{\partial T_P} \dot{V} T_P - Q\dot{V} + A - J + S \tag{4}$$

$$V\frac{\partial E_R^g}{\partial t} = \frac{\partial}{\partial m_o}\left(r^{\delta-1}k_R^g\frac{\partial E_R^g}{\partial r}\right) - \frac{4}{3}E_R^g\dot{V} - c\sigma_P^g E_R^g + J^g\ ; \qquad g = 1,\ \ldots,\ G \qquad (5)$$

where

$$E_R^g = \int_{h\nu_g}^{h\nu_{g+1}} dh\nu\ E_R(r,h\nu,t)$$

$$A^g = c\sigma_P^g E_R^g$$

$$J^g = \frac{8\pi k_B T_P^4}{c^2 h^3}\sigma_P^g \int_{x_g}^{x_{g+1}} dx\ \frac{x^3}{e^x - 1}\ ; \qquad x = \frac{h\nu}{k_B T_P}$$

$$k_R^g = \frac{cV}{3\sigma_R^g}$$

$$A = \sum_{g=1}^{G} A^g$$

$$J = \sum_{g=1}^{G} J^g\ .$$

C_V is the specific heat at constant volume, Q is the artificial viscosity, V is the plasma specific volume, k_P is the plasma thermal conductivity, k_R^g is the radiation conductivity for frequency group g, J^g is the rate of radiation energy emitted by the plasma into group g, S is the rate of internal energy added to the plasma by the target debris and σ_P^g and σ_R^g are the Planck and Rosseland opacities for group g, respectively. In the MF-FIRE code, 20 energy groups are used as shown in Table 2. The expression for the thermal conductivity of the plasma is the theoretical expression developed for electrons interacting with stationary ions [8] as

$$k_P = 20\left(\frac{2}{\pi}\right)^{3/2}\frac{T_P^{5/2}}{\sqrt{m_e}\ e^4(Z + 4)\ \ln\Lambda} \qquad (6)$$

Table 2. Boundaries of Radiation Energy Groups

Group Number	Energy Range (eV)
1	3×10^{-3} - 1
2	1 - 3
3	3 - 5
4	5 - 7.5
5	7.5 - 10
6	10 - 15.6
7	15.6 - 19
8	19 - 25
9	25 - 29.47
10	29.47 - 48.7
11	48.7 - 75
12	75 - 100
13	100 - 125
14	125 - 150
15	150 - 200
16	200 - 300
17	300 - 400
18	400 - 500
19	500 - 1000
20	1000 - 20000

where e is the electron charge, m_e is the electron mass and $\ln \Lambda$ is the Coulomb logarithm.

The multigroup equations are first solved individually and the absorption and emission terms A and J are computed. These terms are then explicitly included in the plasma temperature equation which is solved next. An adjustment is added to the solution of these nonlinear diffusion equations to ensure physical relevance and numerical stability. The radiation diffusion equation is flux-limited. The flux across a zone boundary is not allowed to exceed cE_R, which is the free-streaming limit of radiation flux in a vacuum.

A most important feature of this model is the equation of state and radiative property data. For the MF-FIRE code, these data are stored in tabular form as a function of density and plasma temperature. The tabulated quantities include: charge state $Z(n_P,T_P)$, plasma specific internal energy $e(n_P,T_P)$ and multigroup Planck and Rosseland opacities $\sigma_P^g(n_P,T_P)$, $\sigma_R^g(n_P,T_P)$. These quantities are computed using a semi-classical model of the atom by the code MIXERG [9].

The time required for the deposition of target x-rays into the cavity gas ($\sim 10^{-8}$ sec) is much shorter than the hydrodynamic response time, so the gas is stationary as the x-rays are deposited. Hence, the thermodynamic state of the gas after x-ray deposition can be used as an initial condition in computing the gas response to the exploding target. The MF-FIRE code allows the target x-ray spectrum to be broken up into 20 groups (different from the radiation diffusion group structure) and assumes exponential attenuation of each group, which should be adequate for most target x-ray spectra. The initial x-rays that are photoabsorbed by the gas reduce the number of bound electrons available to interact with subsequent x-rays, so the attenuation coefficient decreases as x-rays are deposited. This is called the x-ray bleaching effect. A method of modifying the photoelectric attenuation coefficient of the gas to account for increasing ionization has been included in the MF-FIRE code [10] to simulate this bleaching effect.

III. Microfireball Calculations and Discussion

We have used the multifrequency approximation for radiation transport with the opacity data from MIXERG to simulate the behavior of fusion target generated microfireballs in the Target Development Facility target chamber filled with 27.3 torr (at 0°C) N_2 gas. This pressure was chosen to give a mass density of 2.25×10^{-5} g/cm^3 to support channel formation [11]. Targets with yields of 50 MJ, 200 MJ and 800 MJ were used. The target chamber is actually a right circular cylinder, but for our one-dimensional spherical fireball calculations we have put the first wall at 1.5, 3 and 6 meters in radius. The details of the input parameters are given in Table 3.

We use the initial pellet x-ray energy spectrum obtained from the PHD-IV code [12] as shown in Fig. 3. Here, 27% of the target yield is released as x-rays and debris. In our calculation the pellet x-ray energy is deposited in the gas at t = 0 sec. Rather than using the dynamic debris attenuation option in MF-FIRE the deposition of the debris energy is simulated by adding the debris energy to the lowest x-ray energy group. This group is strongly attenuated by the gas, thus characterizing the short range of the ion debris. The initial pellet x-ray energy including the simulated debris, the energy deposited in the gas and the unattenuated energy reaching the first wall are summarized in Table 4. Table 4 shows that 67~84% of the pellet x-ray and debris energy is deposited in the gas and that 16~33% escapes to the wall, unattenuated. The energy spectrum of the x-rays incident on the wall at 3 m

Table 3. Input Parameters

Cavity radius (m)	1.5, 3, 6
Gas type	Nitrogen
Gas pressure at 0°C (torr)	27.3
Gas number density (cm^{-3})	9.68×10^{17}
Gas mass density ($g \cdot cm^{-3}$)	2.25×10^{-5}
Target yield (MJ)	50, 200, 800
Initial gas temperature (eV)	0.1

Table 4. Deposition of X-Ray Energy at the Initial Condition (MJ)

		1.5 m	3 m	6 m
50 MJ	Initial energy	13.45	13.45	13.45
	Energy deposition in gas	9.36	10.36	11.27
	Unattenuated energy	4.09	3.09	2.18
200 MJ	Initial energy	53.81	53.81	53.81
	Energy deposition in gas	37.09	41.28	45.02
	Unattenuated energy	16.72	12.53	8.79
800 MJ	Initial energy	215.31	215.31	215.31
	Energy deposition in gas	145.13	163.72	179.56
	Unattenuated energy	70.18	51.59	35.75

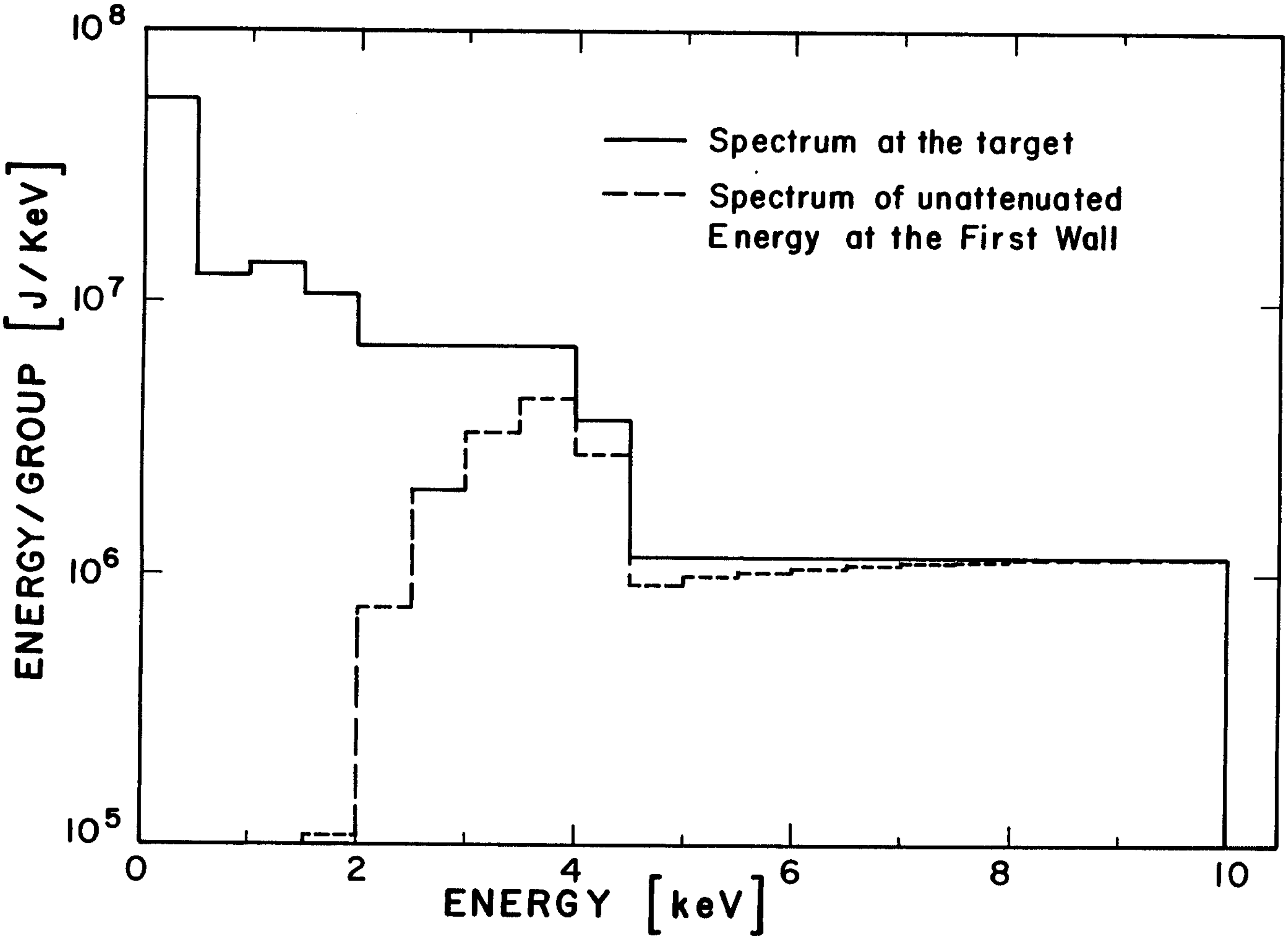

Fig. 3. Target x-ray spectrum used to initialize microfireball calculation for a 200 MJ target yield.

for a 200 MJ yield is also shown in Fig. 3 (dotted line). Figure 3 shows that the N_2 gas is transparent to x-rays with energy greater than 5 keV.

The details of the microfireball behavior for the 200 MJ target yield and 3 m radius chamber are given in Figs. 4 through 8. Plots for the 50 MJ and 800 MJ cases are not qualitatively different. The hydrodynamic motion of the gas is shown in Fig. 4. The radii of the Lagrangian zone boundaries are plotted against time, showing the propagation of the shock front to the wall and reflection off of the wall. Figures 5, 6 and 7 are plots of the plasma temperature, the radiation temperature and the plasma pressure profiles as a function of radius at different times during the shock propagation to the wall. These figures show that there is a small peak around the radius of 20 cm on the profile at 1.80 x 10^{-7} ms. This unreal peak is attributable to overestimation of the x-ray bleaching effect in the region $R \lesssim 20$ cm. However, this peak occurs only at very early times so that its effect on the fireball behavior is negligible. Figure 8 is a plot of the heat flux and mechanical overpressure experienced at the wall as a function of time. The radiation energy reaches the wall in two distinct pulses. The largest instantaneous flux, 485 kW/cm^2, occurs very early in time, 5.22 x 10^{-8} sec, and the second largest instantaneous heat flux, 3.78 kW/cm^2, occurs at almost the same time when the wall experiences the maximum overpressure, 0.45 ms. The peak heat flux of the first pulse is much larger but its pulse width is much smaller than those of the second pulse. Figures 9 and 10 are the time-integrated radiation spectra at the wall just after the first and second pulses, respectively. These figures show that the first pulse is composed mainly of hard x-rays (> 500 eV). The second pulse is composed of soft x-rays

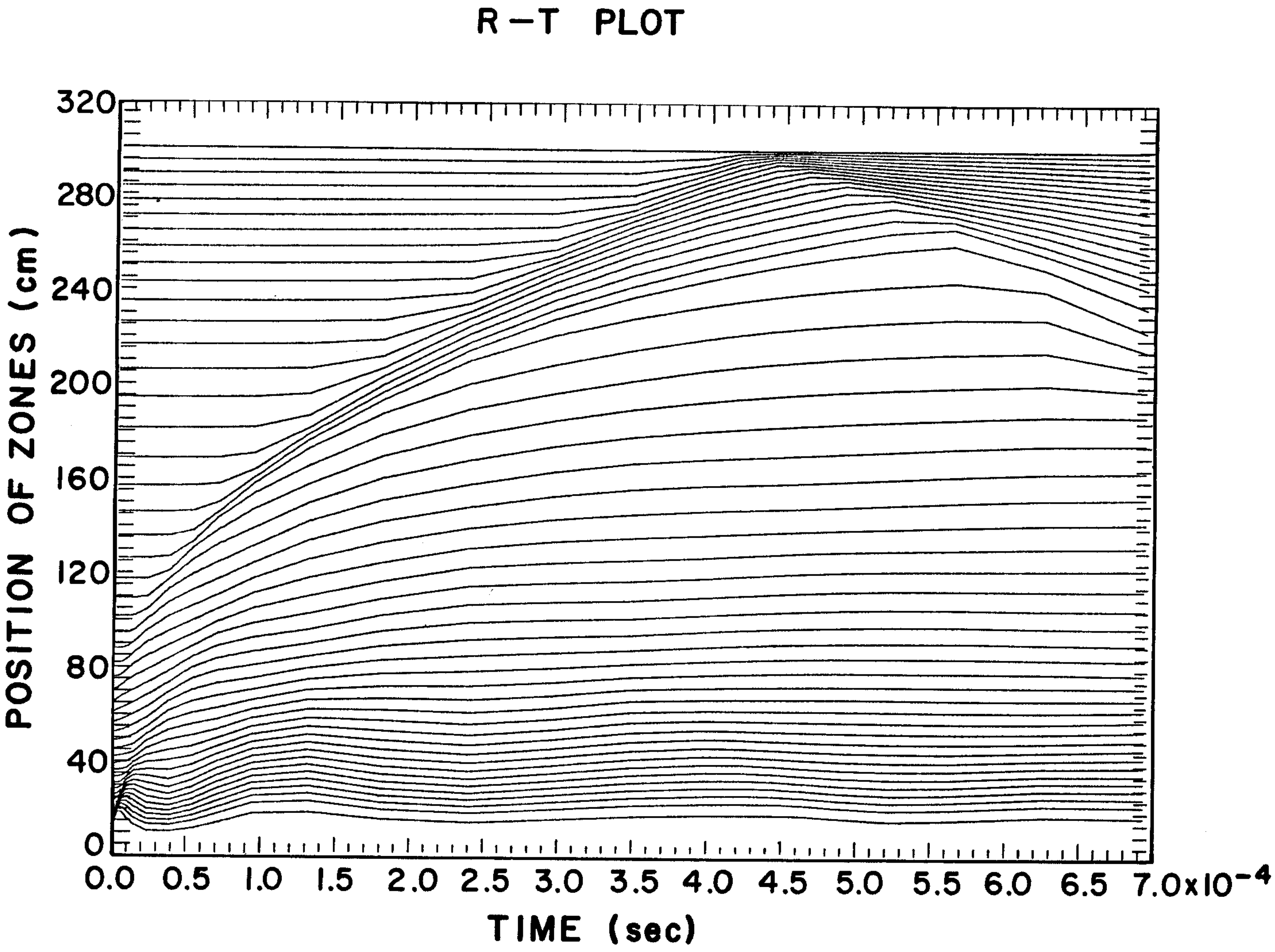

Fig. 4. Hydrodynamic motion of Lagrangian zone boundaries plotted against time. Target yield is 200 MJ in 27.3 torr (at 0°C) of N_2 gas.

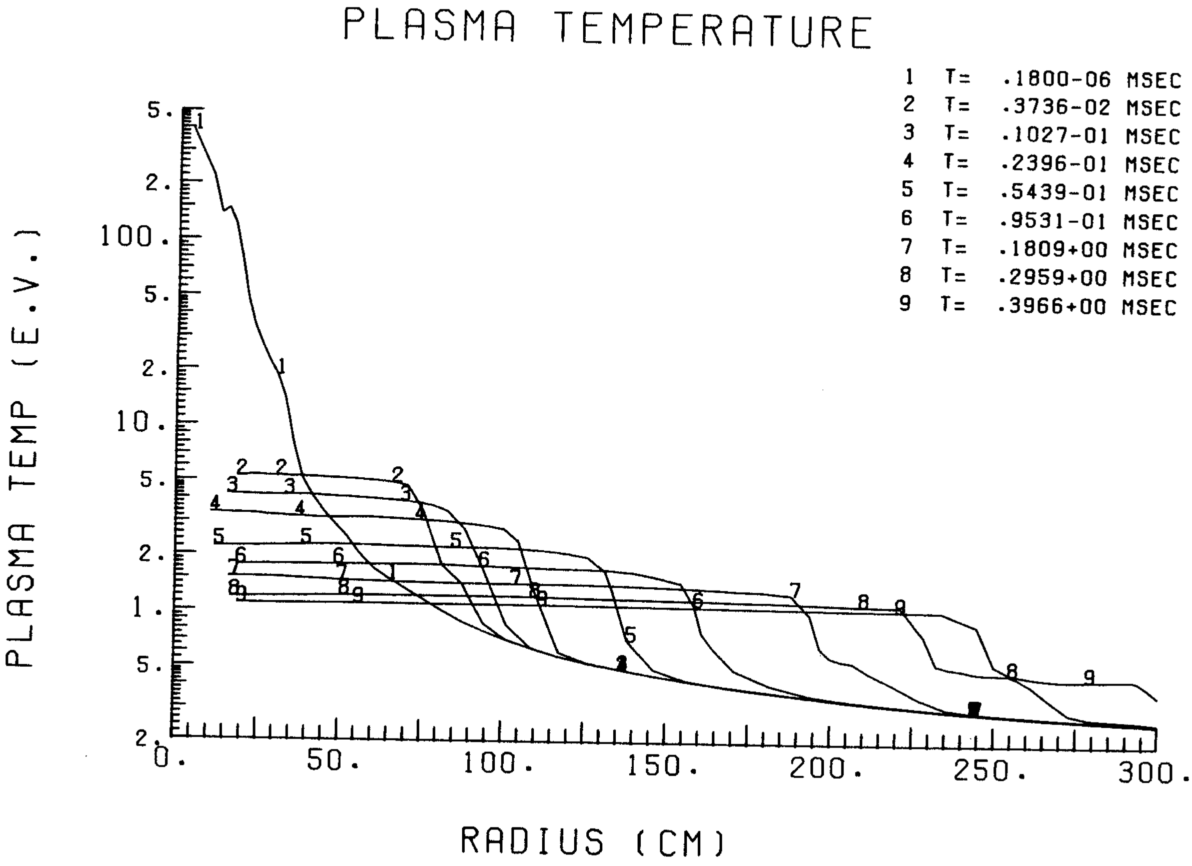

Fig. 5. Plasma temperature profiles at various times for a 200 MJ target yield in 27.3 torr (at 0°C), N_2 gas.

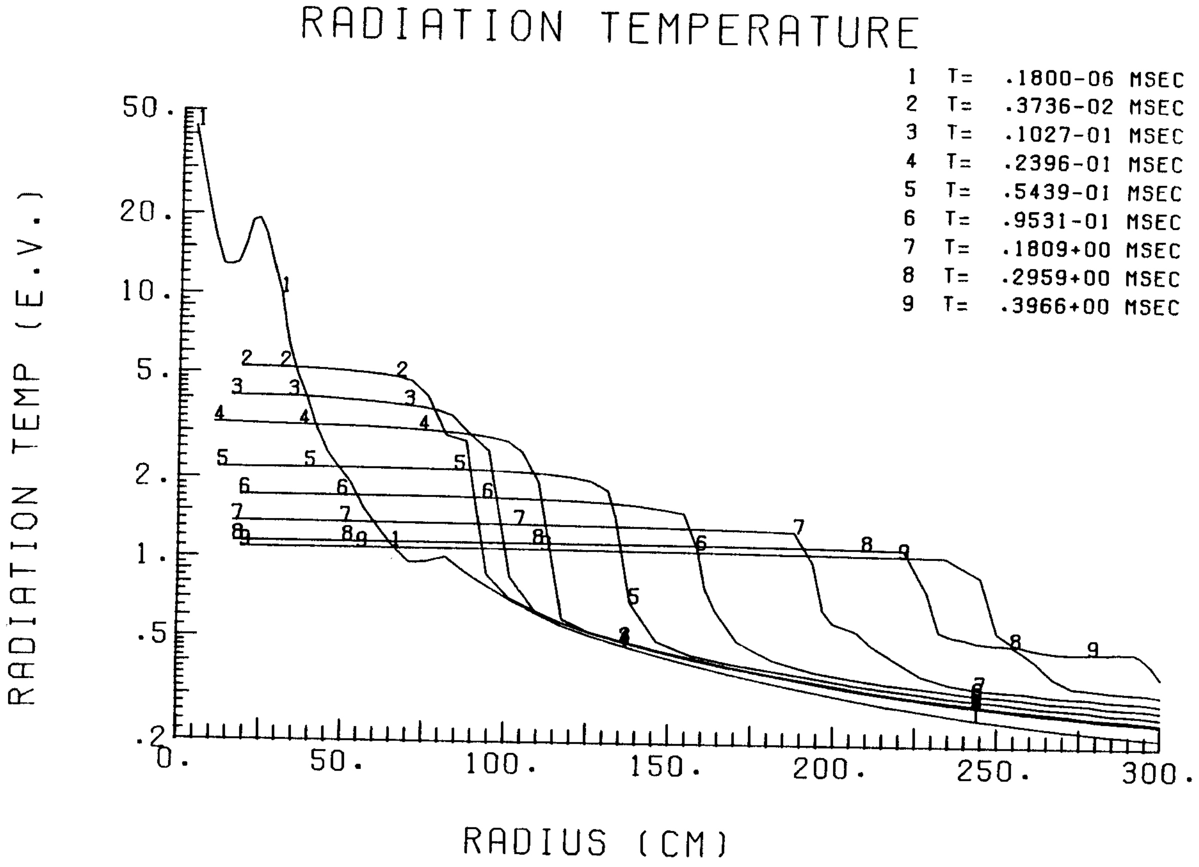

Fig. 6. Radiation temperature profiles at various times for a 200 MJ target yield in 27.3 torr (at 0°C), N_2 gas.

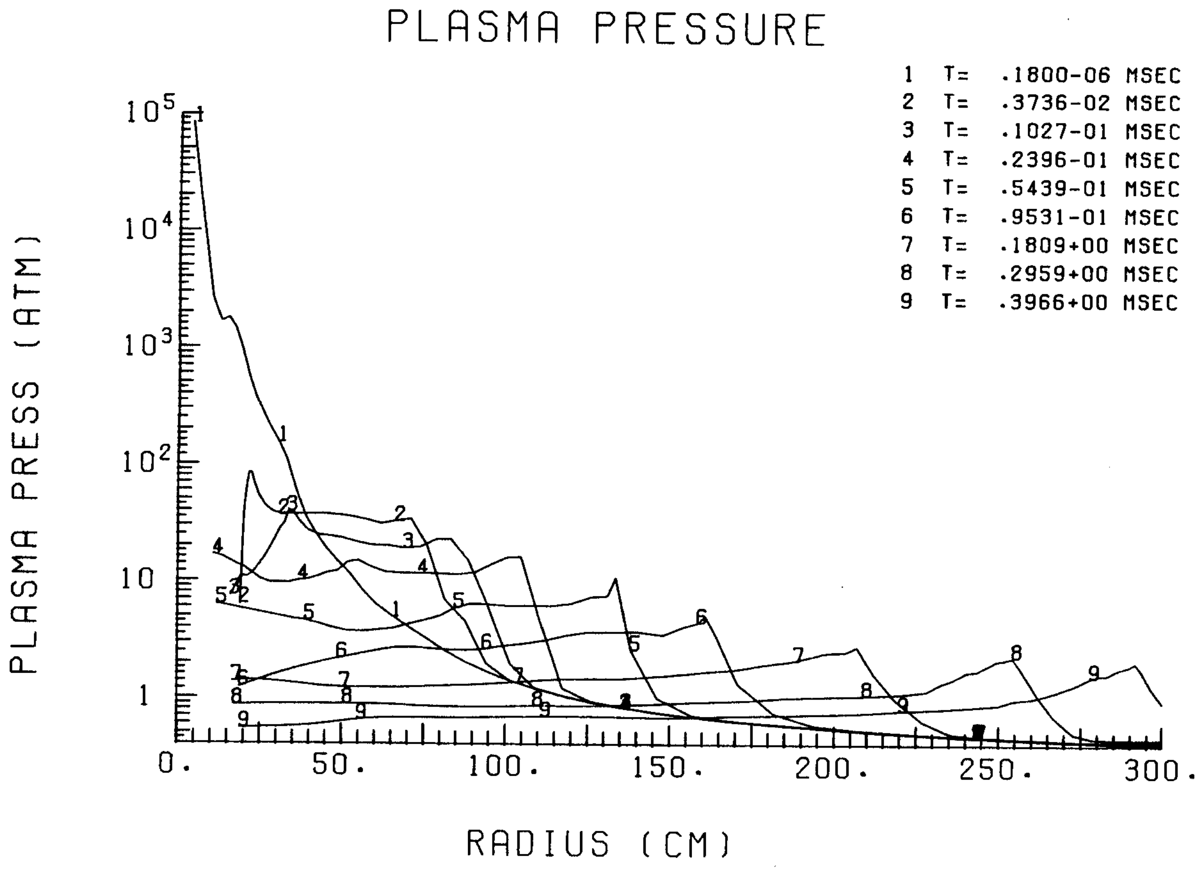

Fig. 7. Plasma pressure profiles at various times for a 200 MJ target yield in 27.3 torr (at 0°C), N_2 gas.

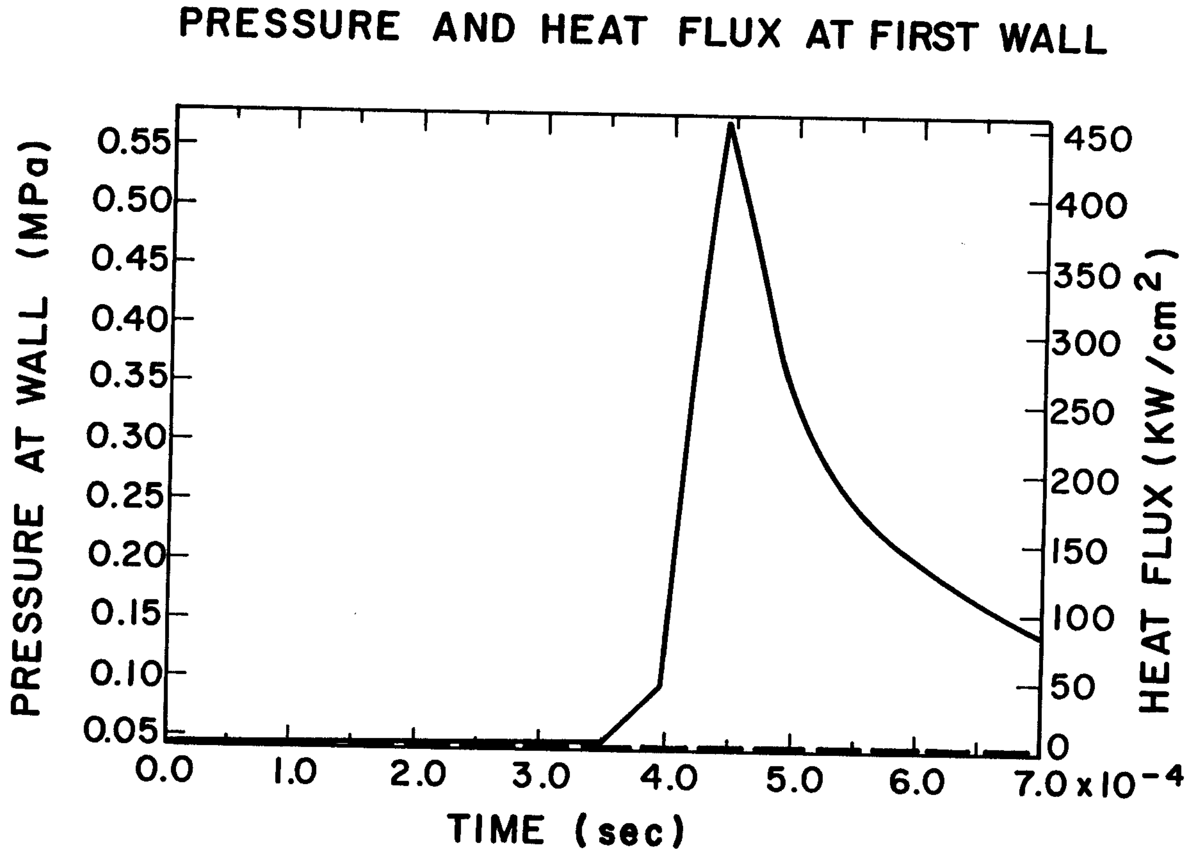

Fig. 8. Overpressure and heat flux at a 3 meter radius first wall of a cavity filled with 27.3 torr (at 0°C) of N_2 gas. Target yield is 200 MJ.

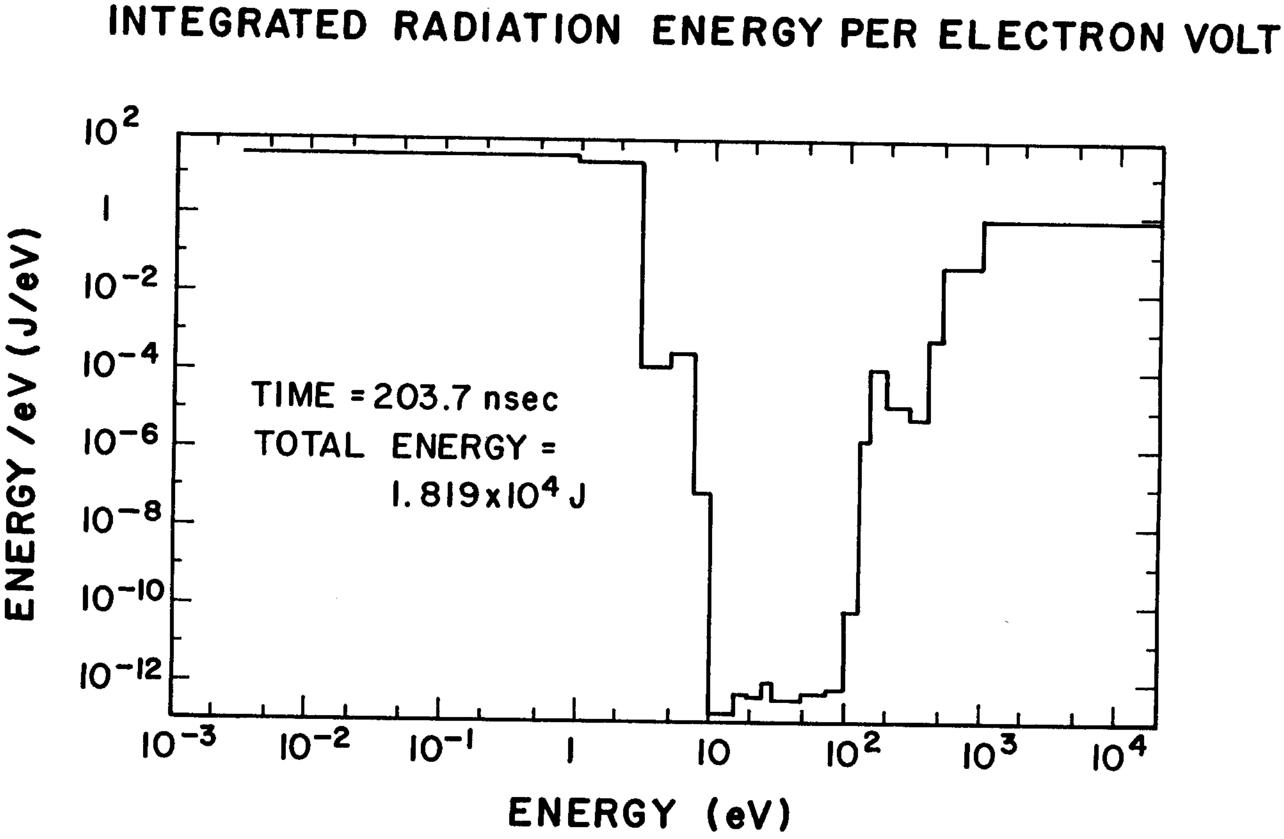

Fig. 9. Time-integrated radiation energy spectrum after the first pulse at a 3 meter radius first wall of a cavity filled with 27.3 torr (at 0°C) of N_2 gas. Target yield is 200 MJ.

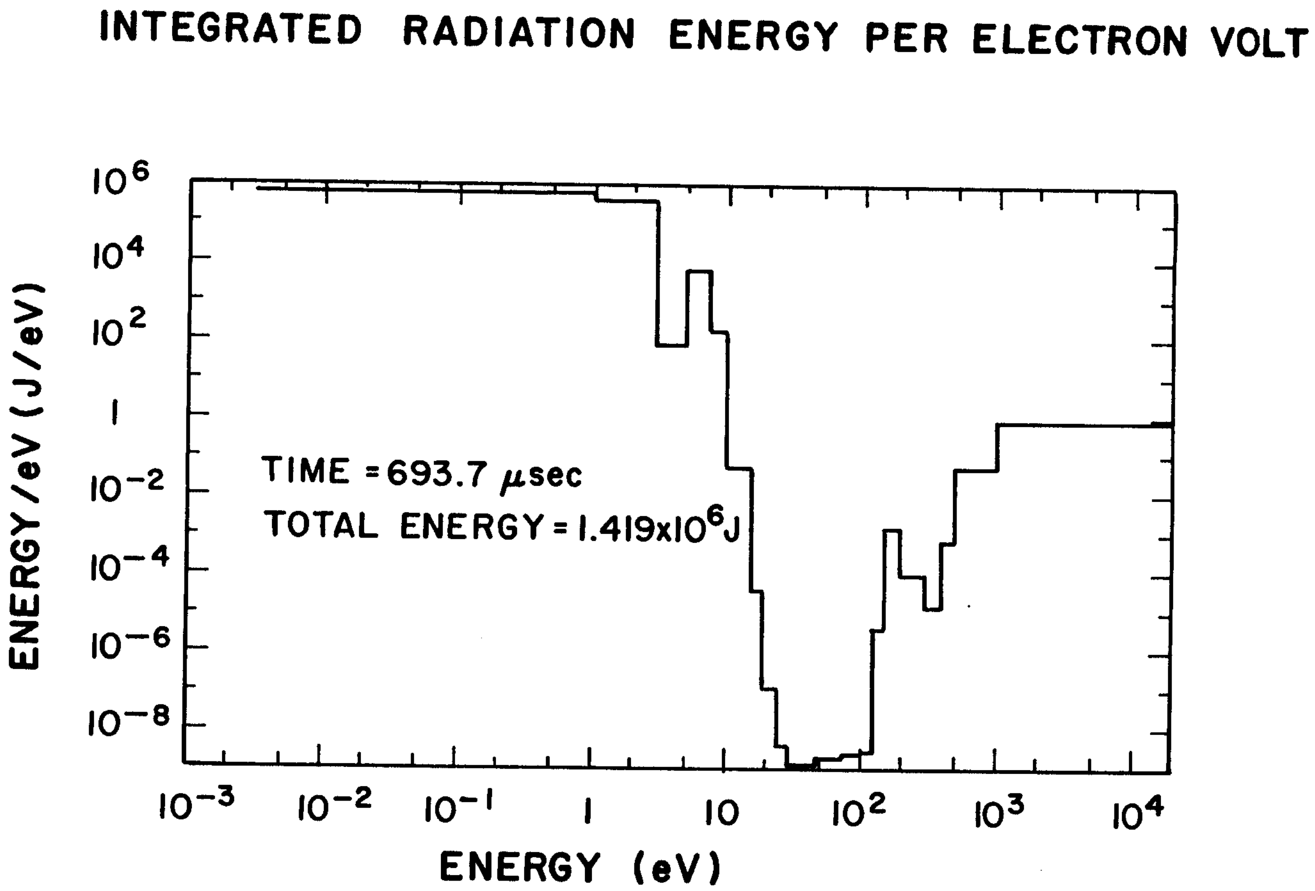

Fig. 10. Time-integrated radiation energy spectrum after the second pulse at a 3 meter radius first wall of a cavity filled with 27.3 torr (at 0°C) of N_2 gas. Target yield is 200 MJ.

(< 10 eV). The radiated energy of the first pulse is much smaller than that of the second pulse by a factor of a hundred.

The energy radiated to the wall, the maximum overpressure at the wall, the time of the maximum overpressure, the peak heat fluxes and the times of the peak heat fluxes for all cases are given in Tables 5 through 10. The characteristics of the radiation hydrodynamics strongly depend on the opacity data which are functions of the plasma density, the plasma temperature and the radiation energy. The opacity of each radiation energy group has a different dependence from those of the other groups. Hence, it is very difficult to establish a scaling law relating the results to radius or target yield. For example, the result for the 800 MJ, 1.5 m radius case is very different from simple expectation. The energy radiated to the wall increases with increasing radius. This is an artifact of the way the calculations were performed. The calculation is stopped just after the maximum overpressure occurs at the wall, because the one-dimensional spherical model does not accurately represent the reflection of a spherical blast wave from a non-spherical surface. The time of the calculation is longer for larger radius cases so that there is more time for the plasma to emit radiation and to cool. Tables 6 and 7 show that larger overpressure occurs earlier at the wall for larger target yield and smaller radius. This is to be expected. The peak heat flux of the first pulse is much larger and its pulse width is much smaller than the second pulse for all cases except for the 800 MJ, 1.5 m case in Tables 8 and 9. The times of the peak heat flux of the first pulse are given in Table 10. Table 10 shows that the first pulse reaches the wall at the same time for different target yield cases. This means that the hard x-rays (> 500 eV) reach the wall through almost free-streaming. The low opacity of the N_2 gas for the

Table 5. Energy Radiated to Wall (MJ)

		Yield		
		50 MJ	200 MJ	800 MJ
Radius	1.5 m	0.198	0.480	45.9
	3 m	0.862	1.56	2.35
	6 m	2.86	4.43	5.35

Table 6. Maximum Overpressure (MPa)

		Yield		
		50 MJ	200 MJ	800 MJ
Radius	1.5 m	1.17	5.89	5.42
	3 m	0.199	0.624	2.96
	6 m	0.0668	0.134	0.365

Table 7. Time of Maximum Overpressure (ms)

		Yield		
		50 MJ	200 MJ	800 MJ
Radius	1.5 m	0.170	0.0769	0.0253
	3 m	0.673	0.433	0.225
	6 m	2.17	1.58	1.06

Table 8. Peak Heat Flux (kW•cm^{-2})

		Yield		
		50 MJ	200 MJ	800 MJ
Radius	1.5 m	74.6 4.36	2980 178	1620 4940
	3 m	13.4 2.49	485 3.78	429 15.7
	6 m	2.34 0.310	72.7 1.34	83.9 2.94

(*)The upper and lower values correspond to the first and second pulses, respectively.

Table 9. Pulse Width (μs)

		Yield		
		50 MJ	200 MJ	800 MJ
Radius	1.5 m	0.13 260	0.190 15	0.168 10
	3 m	0.291 400	0.31 450	0.209 80
	6 m	0.580 1000	0.488 700	0.30 500

(*)The upper and lower values correspond to the first and second pulses, respectively.

Table 10. Time of the First Peak Heat Flux (x 10^{-8} sec)

	1.5 m	3 m	6 m
50 MJ	2.90	5.39	10.25
200 MJ	2.69	5.22	9.73
800 MJ	2.26	5.59	10.23

hard x-rays induces the first pulse. The first pulse cannot be predicted by using the two temperature approximation where frequency-averaged values of the opacity are used [13]. This is a significant difference from our earlier publications using the two temperature model and is qualitatively in agreement with the work of Sweeney and Cook [14]. The large energy radiated to the wall and the large heat flux of the second pulse for the 800 MJ, 1.5 m case is attributable to the high transparency of the N_2 gas for the x-rays (3 eV $< E_R <$ 100 eV) under the conditions of plasma density and plasma temperature for this case. Since a large amount of energy is released to the wall as radiation, the maximum overpressure is actually smaller in this case than in the case of smaller yields. This will be discussed more fully later in this paper.

It is known that the shock front breaks away from a fireball as the fireball grows. Figures 11, 12 and 13 show the position of the shock front and the fireball boundary as a function of time for the 50 MJ, 200 MJ and 800 MJ cases and wall radius of 6 meters. It is shown that the breakaway occurs around 0.1 ms for all three of these cases. The radius at which the breakaway occurs is about 1.0 meter for the 50 MJ yield, 1.5 meters for the 200 MJ yield and 2.5 meters for the 800 MJ yield. It is interesting to note that the (800 MJ, 1.5 m) combination of target yield and cavity radius is a case that corresponds to the situation where the shock front has not broken away from the fireball before reaching the first wall. This explains the peculiar small value of overpressure for this case noted earlier. In all of the other 8 cases the fireball has been able to convert its energy into a strong shock wave before reaching the wall. We find that this breakaway can be related to the formation of a shock that obeys strong shock theory [15], which predicts that the shock front position is given by the expression,

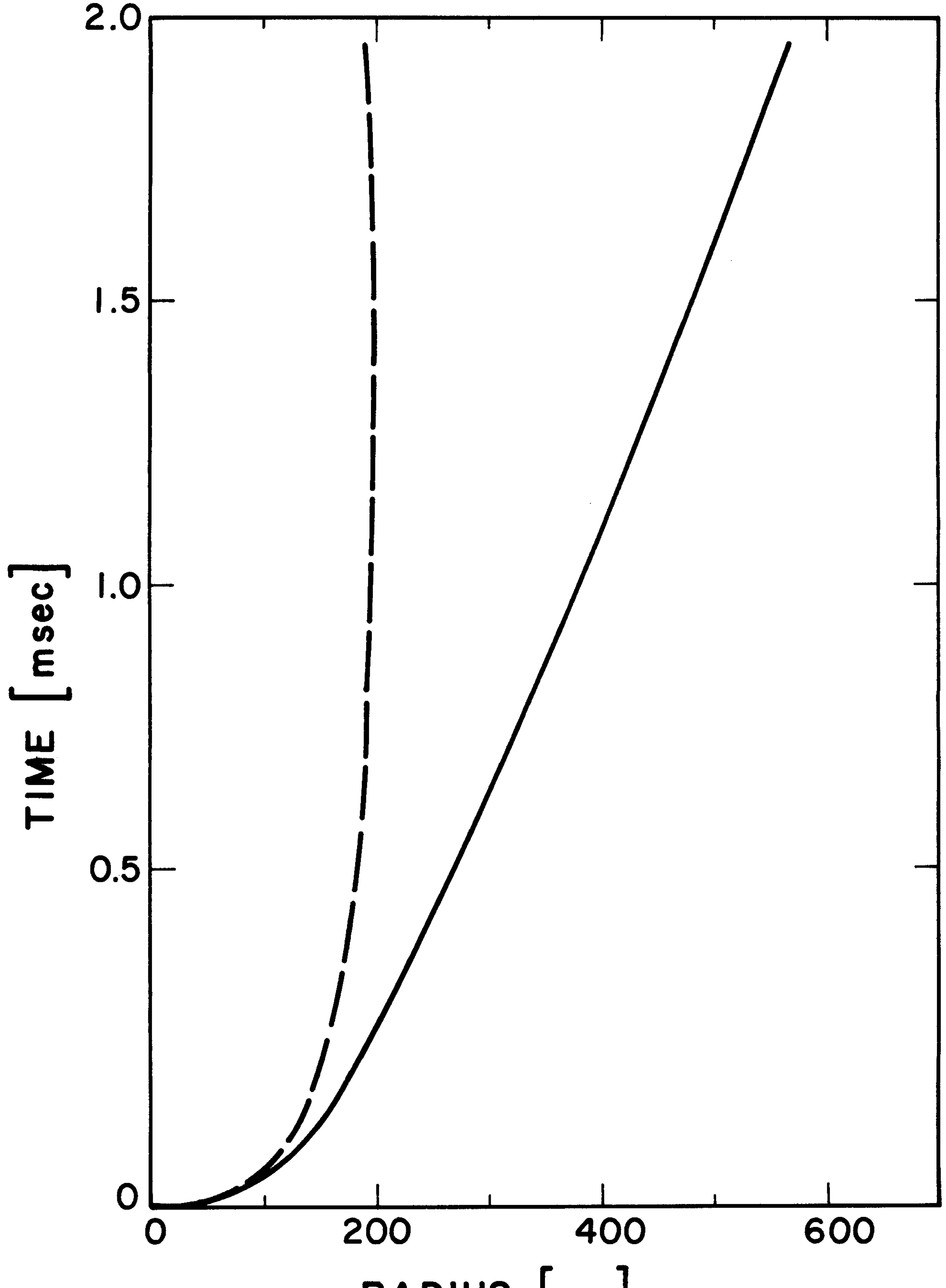

Fig. 11. Trace of the shock front and the fireball boundary for a 50 MJ target yield in 27.3 torr (at 0°C), N_2 gas.

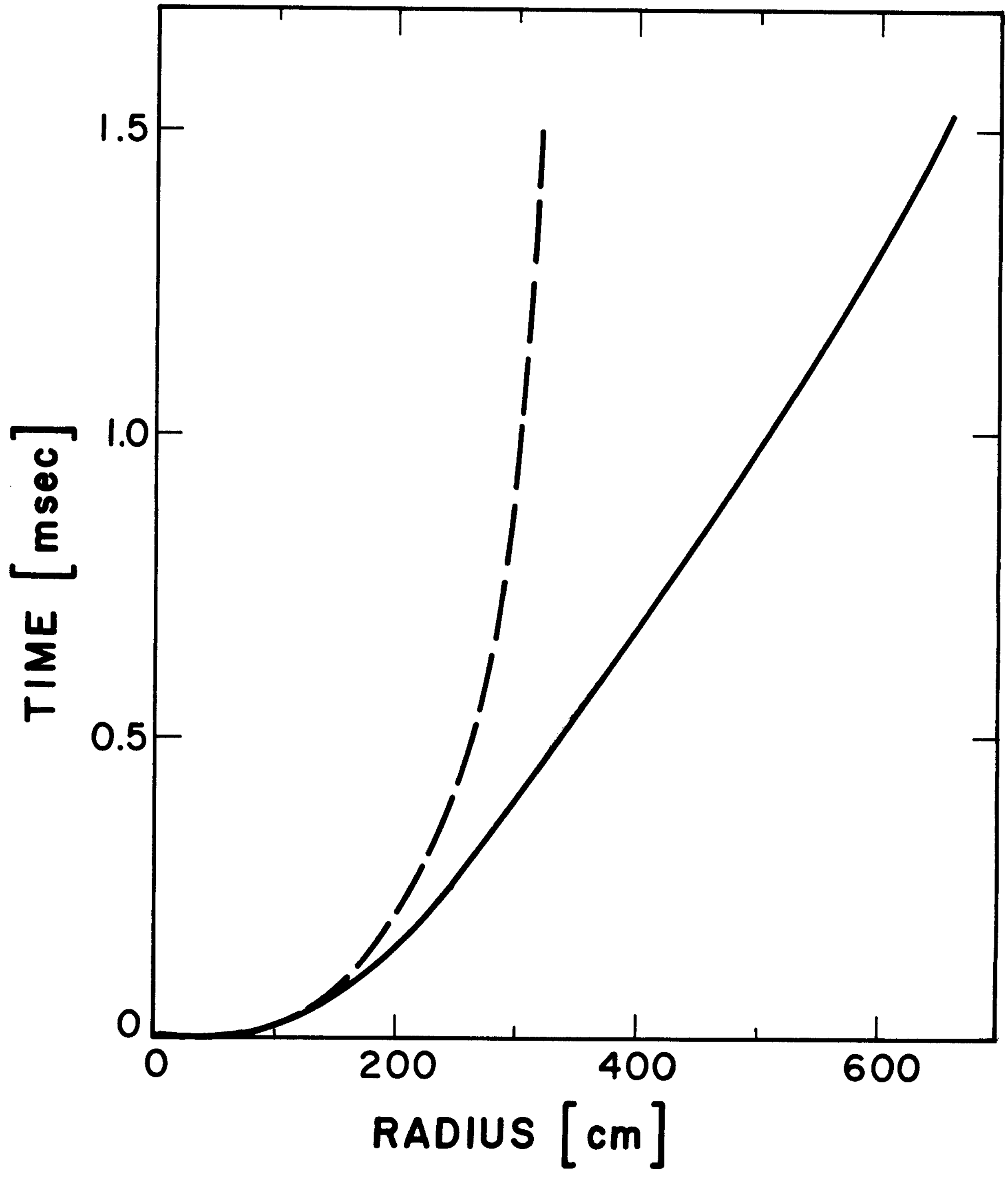

Fig. 12. Trace of the shock front and the fireball boundary for a 200 MJ target yield in 27.3 torr (at 0°C), N_2 gas.

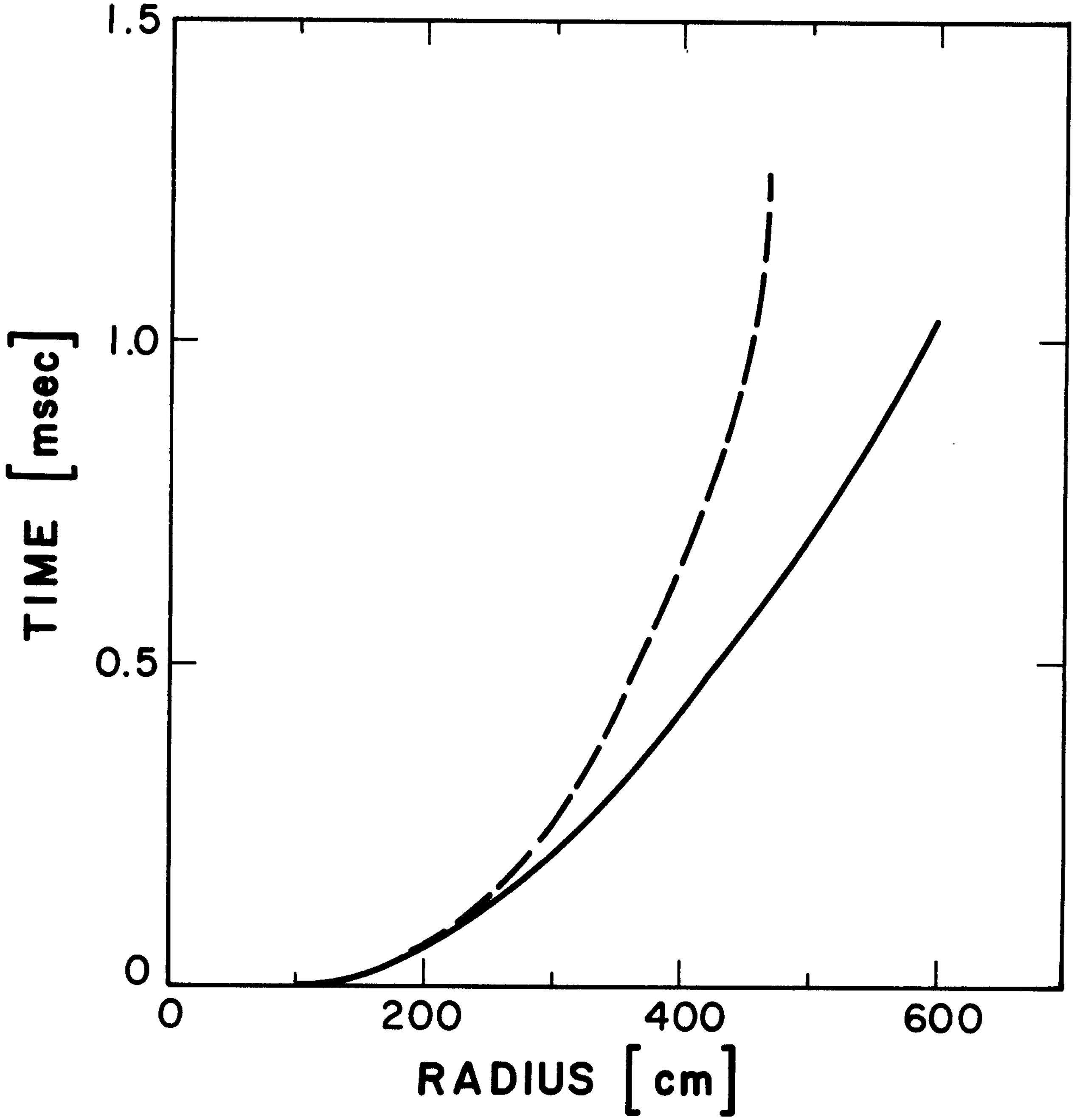

Fig. 13. Trace of the shock front and the fireball boundary for an 800 MJ target yield in 27.3 torr (at 0°C), N_2 gas.

$$R(t) = \left[\alpha(\gamma)\,\frac{E}{\rho_0}\right]^{1/5} t^{2/5} \; ; \qquad \frac{5}{2}\log R = \frac{1}{2}\log\left(\alpha\,\frac{E}{\rho_0}\right) + \log t \qquad (7)$$

where E is the explosion energy, ρ_0 is the density of the gas and $\alpha(\gamma)$ is a function of the specific heat ratio. Figures 14, 15 and 16 are log $R^{5/2}$ vs. log t plots of the shock propagation for the 50 MJ, 200 MJ and 800 MJ cases. The numerical results which lie on a line inclined at 45° to the coordinate axes indicate good agreement with the theoretical prediction. These figures show that the strong shock is formed around 0.1 ms, when the breakaway occurs, and it propagates in the gas until around 1 ms. Then, the shock becomes weak and its propagation is described by weak-shock theory [16]. Weak shocks propagate at velocities very close to the sound speed of the gas.

The simultaneity of the breakaway of the shock front from the fireball boundary and the formation of the strong shock front can be explained by investigating profiles of the Rosseland opacities as a function of radiation energy groups at the fireball boundary. Table 11 shows changes of the Rosseland opacities at the fireball boundary before, during and after the breakaway. A circle (o), a cross (x) and an angle (^) represents sharp increase, sharp decrease and decrease with a small peak at the boundary as shown below Table 11. A solid bar in the tables indicates the x-ray energy spectrum and a circle on that shows the location of the peak. Temperatures inside and outside the fireball are also shown there. The Rosseland opacity is used as a measure of an optical thickness of the gas [17]. As the Rosseland opacity increases, i.e. the optical thickness increases, the radiation diffusion is a more dominant process in the radiation transport. The Rosseland opacities of the energy groups in the radiation energy spectrum increase sharply at the fireball boundary at 3.18×10^{-7} s, before the break-

Table 11. Change of Rosseland Opacity at the Edge of Fireball for 200 MJ, Nitrogen, 27 Torr Case

Time (sec)		3.18×10^{-7}		5.44×10^{-5}		7.53×10^{-4}	
Temp. in Fireball		~ 10 eV		~ 2.2 eV		~ 1.0 eV	
Temp out of Fireball		~ 0.25 eV		~ 0.25 eV		~ 0.25 eV	
G1	3×10^{-3} - 1	^		^		^	
2	1 - 3	^		^		^	o
3	3 - 5	o		o	o	o	
4	5 - 7.5	^		^		^	
5	7.5 - 10	^		^		^	
6	10 - 15.6	o		o		o	
7	15.6 - 19	o		o		o	
8	19 - 25	o		o		x	
9	25 - 29.47	o		o		x	
10	29.47 - 48.7	o	o	o		x	
11	48.7 - 75	o		x		x	
12	75 - 100	o		x		x	
13	100 - 125	o		x		x	
14	125 - 150	o		x		x	
15	150 - 200	o		x		x	
16	200 - 300	x		x		x	
17	300 - 400	x		x		x	
18	400 - 500	x		x		x	
19	500 - 1000	x		x		x	
20	1000 - 20000	x		x		x	

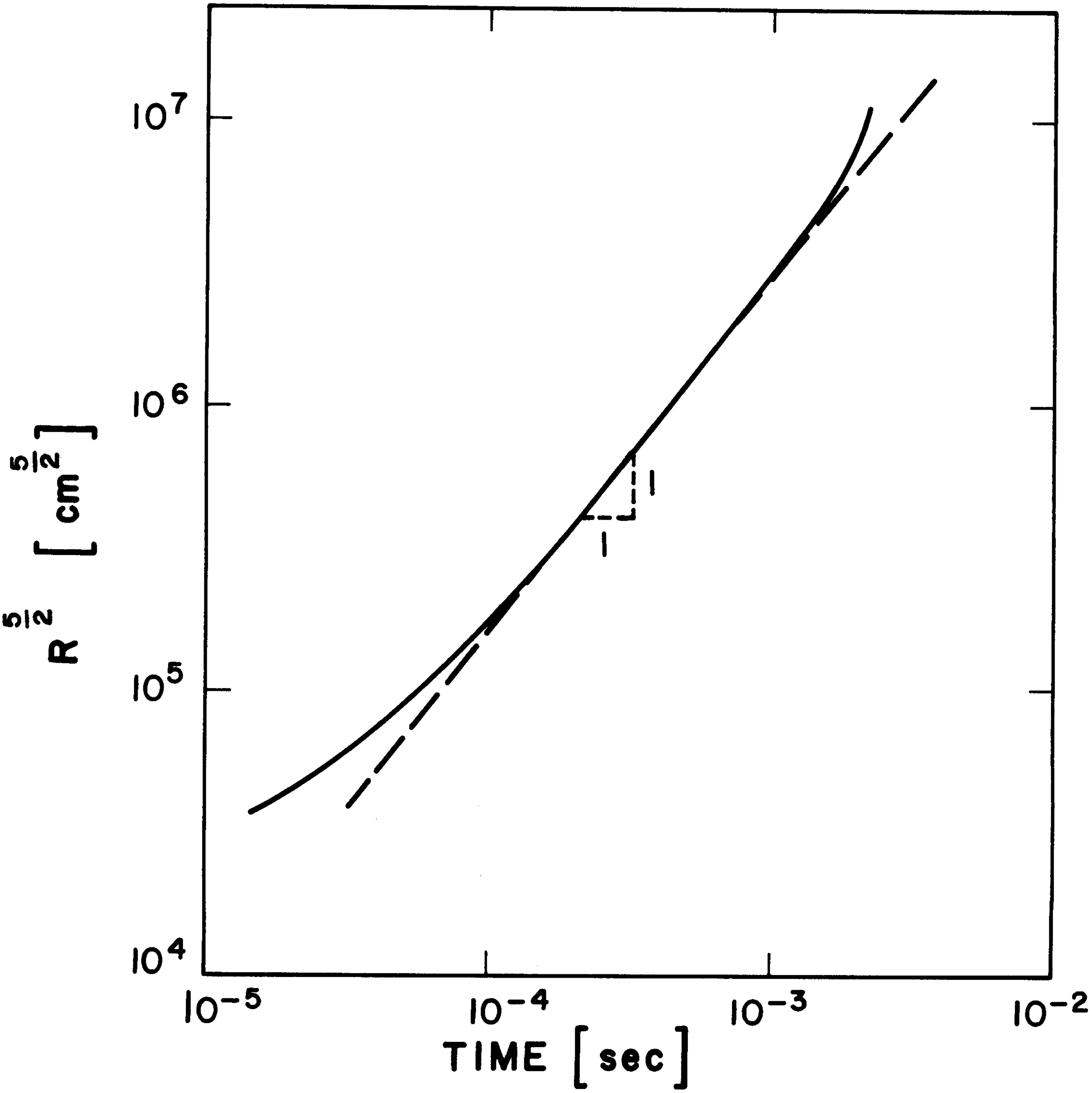

Fig. 14. Log $R^{5/2}$ vs. log t plot of the shock propagation for a 50 MJ target yield in 27.3 torr (at 0°C), N_2 gas.

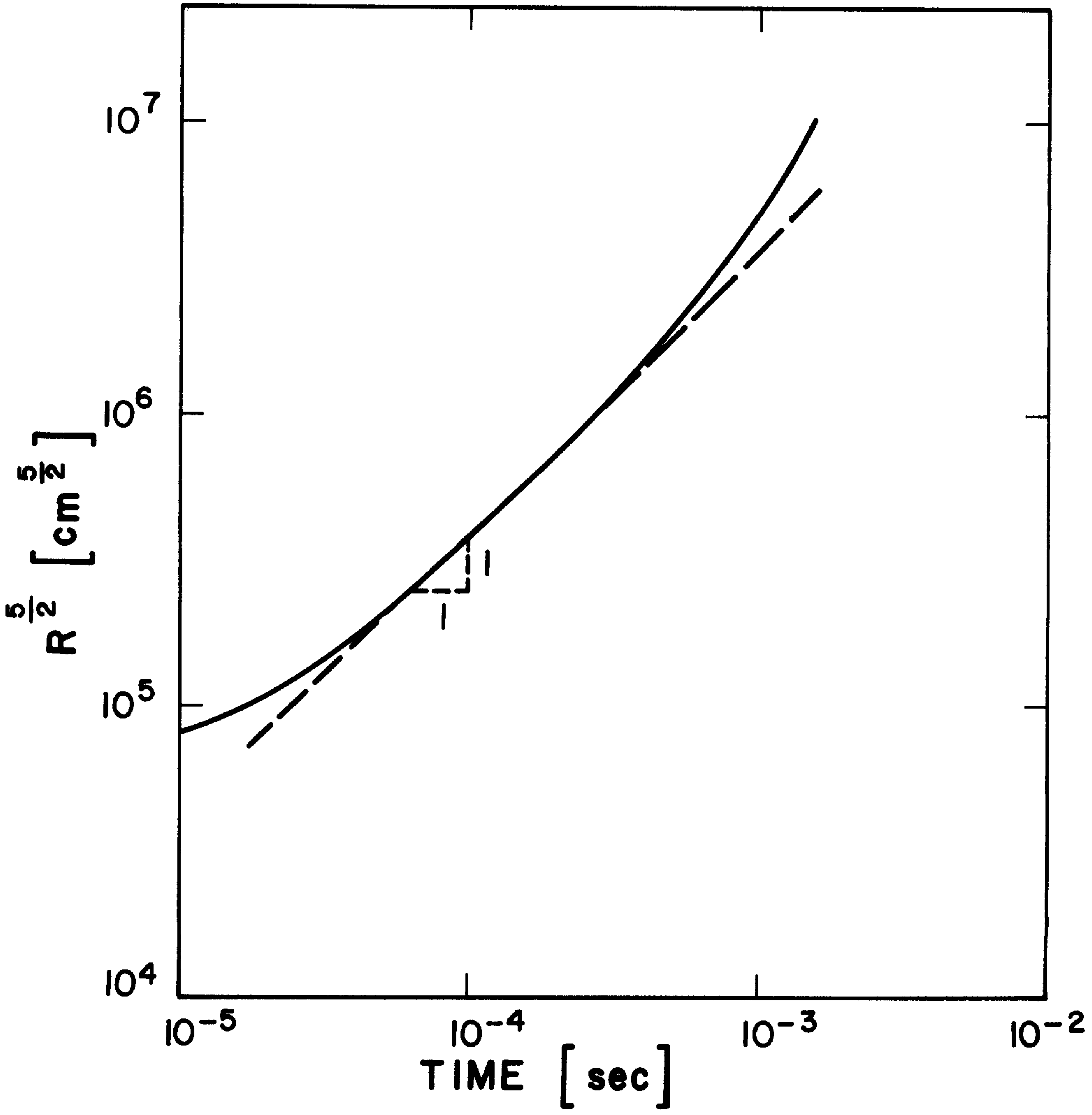

Fig. 15. Log $R^{5/2}$ vs. log t plot of the shock propagation for a 200 MJ target yield in 27.3 torr (at 0°C), N_2 gas.

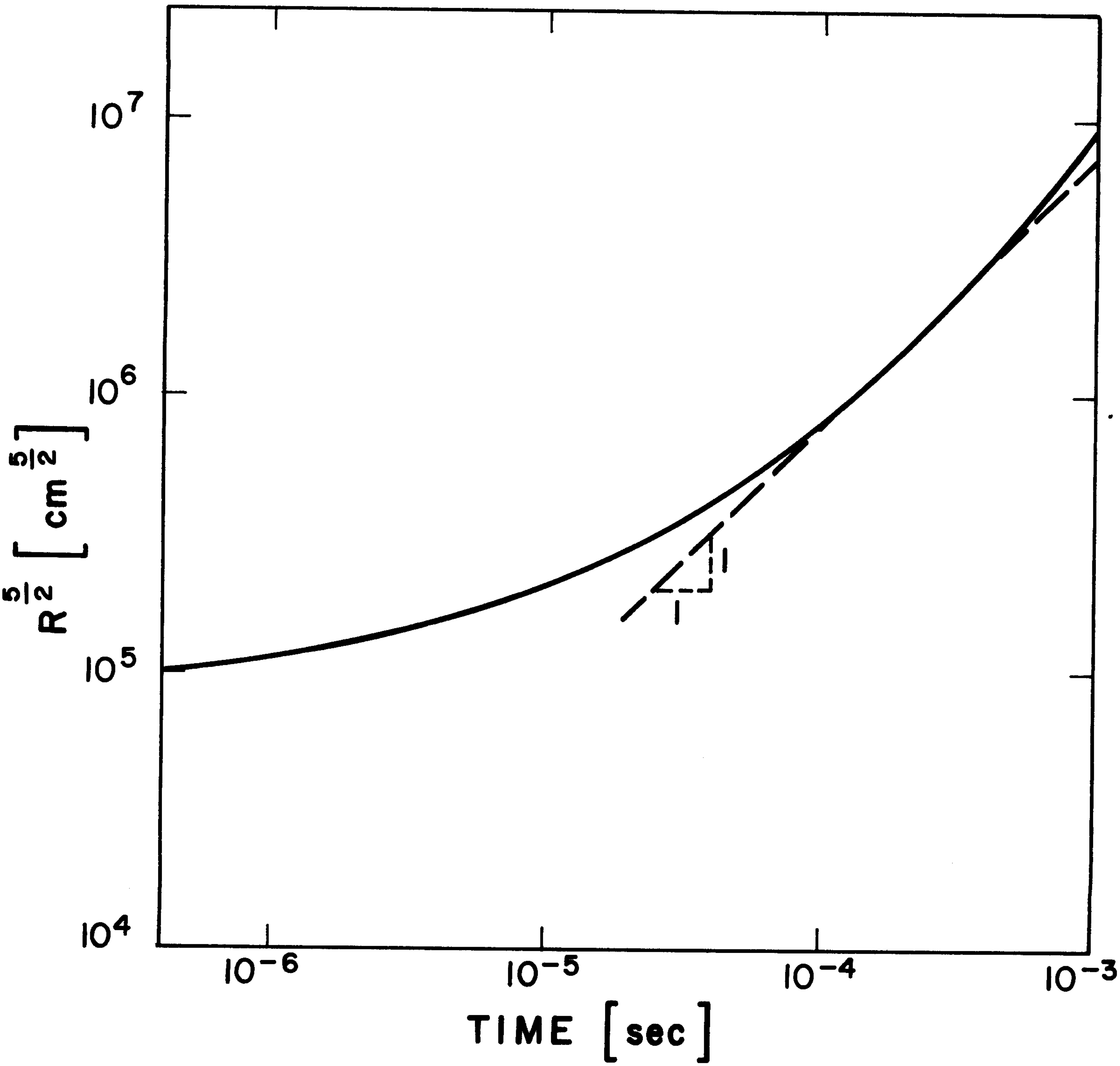

Fig. 16. Log $R^{5/2}$ vs. log t plot of the shock propagation for an 800 MJ target yield in 27.3 torr (at 0°C), N_2 gas.

away, as shown in Table 11. In this case the radiation emitted by the fireball is strongly absorbed around the boundary. This means that the initial fireball expansion is due to radiation diffusion in the gas, a process which occurs much more rapidly than the hydrodynamic response of the gas. Hence, there is insufficient time to form a strong shock. As the fireball grows, its radiation energy spectrum becomes softer as shown in Table 11. In the low energy region, the Rosseland opacity of the surrounding gas decreases at the boundary so that the gas becomes transparent to radiation. At this stage, the expansion velocity of the fireball due to the radiation diffusion decreases. Once the fireball has cooled enough that the radiation diffusion velocity is the same as the shock velocity, a strong shock is formed. This now propagates ahead of the expanding fireball, i.e. the breakaway occurs.

Equivalent strong shock explosion energies for the 50 MJ, 200 MJ and 800 MJ cases have been calculated by using Eq. (7) from a straight part of the log $R^{5/2}$ - log t plots in Figs. 14, 15 and 16. They are given in Table 12. The equivalent explosion energy is always smaller than the energy deposited in the gas given in Table 4. This is because the energy deposited outside the fireball and the energy leaking as radiation from the shock front are not used to form the strong shock. The degree to which this equivalent explosion energy is less than the actual deposited energy shows the relative importance of radiative transfer to the fireball dynamics. Hence, we see that the larger target yield of 800 MJ most closely resembles a strong shock and radiation plays the least dominant role. Conversely, the low energy yield of 50 MJ produces a strong shock front trajectory that significantly underpredicts the target yield. This analysis indicates that great care must be taken if one

Table 12. Equivalent Initial Energy Obtained from Strong Shock Theory (MJ)

	50 MJ	200 MJ	800 MJ
E_0	5.25	26.7	142
E_{Dep}	11.27	45.02	179.56
E_0/E_{Dep}	0.52	0.59	0.79

wishes to use the strong shock trajectory as a diagnostic for target yield as has previously been done for atmospheric tests of nuclear weapons.

IV. Summary and Conclusions

The response of a nitrogen target chamber gas to fusion target explosions is calculated for the light ion beam driven target development facility, using the MF-FIRE code. In the MF-FIRE code, the one-fluid hydrodynamic approximation is used in the one-dimensional equation of motion in Lagrangian coordinates, the plasma electrons and ions are assumed to be in equilibrium with each other in the plasma temperature equation and the multifrequency approximation (20 groups) is used in the radiation diffusion equation. The multifrequency opacity data are provided by the MIXERG code. The initial pellet x-ray energy spectrum obtained from the PHD-IV code is used as an input in these calculations. Then, the thermodynamic state of the gas after the deposition of those x-rays is used as an initial condition in computing the gas response to the exploding target.

Target yields of 50 MJ, 200 MJ and 800 MJ are considered for target chambers 1.5 m, 3 m and 6 m in radius which are filled with N_2 gas at a density of 2.25×10^{-5} grams/cm^3 (27.3 torr at 0°C). The shock propagation, the behavior of the fireball, the energy radiated to the first wall, the maximum overpressure and the heat flux at the wall are obtained for these cases. Two pulses of radiation are observed in the calculations, the first of which is composed mainly of hard x-rays (> 500 eV) and cannot be predicted by a two temperature calculation. This information can now be used to calculate the mechanical response of the first wall, i.e. mechanical and thermal stresses. Finally, the breakaway of the shock front from the fireball boundary and the formation of a strong shock are discussed. It is confirmed that the strong shock is formed when the breakaway occurs. The mechanism of the breakaway and the formation of the strong shock is described by investigating the profiles of the opacities of radiation energy groups in the radiation energy spectrum at the fireball boundary. It is noted that the strong shock trajectory underestimates the target yield, hence care should be exercised when using this as a yield diagnostic.

Acknowledgment

This work was supported by Sandia National Laboratory under contract number 16-9850. The first author was supported by the Rotary Club of Japan.

References

[1] Yonas, G., "Inertial Fusion Based on Pulsed Power," Proc. of 9th International Conf. on Plasma Physics and Controlled Nuclear Fusion Research, Baltimore, MD, October 1982.

[2] Moses, G.A., R.R. Peterson, R.L. Engelstad, E.G. Lovell, G.L. Kulcinski, K.J. O'Brien, A.M. White, J.J. Watrous, and D.L. Cook, "Light Ion Fusion Target Development Facility Preconceptual Design," Proc. of the 5th Top. Mtg. on the Tech. of Fusion Energy, Knoxville, TN, April 1983. Also, University of Wisconsin Fusion Engineering Program Report UWFDM-521.

[3] Peterson, R.R., and G.A. Moses, "Target Explosion Generated Fireballs in the Nitrogen Filled Target Chamber of the Light Ion Fusion Target Development Facility," Proc. of the 5th Top. Mtg. on the Tech. of Fusion Energy, Knoxville, TN, April 1983. Also, UWFDM-515.

[4] Peterson, R.R., G.W. Cooper, and G.A. Moses, "Cavity Gas Analysis for Light Ion Beam Fusion Reactors," Nucl. Tech./Fusion 1, 377 (1981).

[5] Moses, G.A., and R.R. Peterson, "First Wall Protection in Particle Beam Fusion Reactors by Inert Cavity Gases," Nucl. Fusion 20, 849 (1980).

[6] Moses, G.A., T.J. McCarville, and R.R. Peterson, "Documentation for MF-FIRE, A Multifrequency Radiative Transfer Version of FIRE," University of Wisconsin Fusion Engineering Program Report UWFDM-458 (March 1982).

[7] Von Neumann, J. and R. Richtmyer, J. Appl. Phys. 21, 232 (1950).

[8] Spitzer, L., Physics of Fully Ionized Gases, Second Edition, Interscience Publishers, New York (1962), p. 144.

[9] Peterson, R.R., and G.A. Moses, "MIXERG - An Equation of State and Opacity Computer Code," University of Wisconsin Fusion Engineering Program Report UWFDM-464 (March 1982).

[10] McCarville, T.J., G.A. Moses, G.L. Kulcinski, "A Model for Depositing Inertial Confinement Fusion X-Rays and Pellet Debris into a Cavity Gas," University of Wisconsin Fusion Engineering Program Report UWFDM-406 (April 1981).

[11] Freeman, J.R., L. Baker, and D.L. Cook, "Plasma Channels for Intense Light Ion Beam Reactors," Nucl. Fusion 22, 383 (1982).

[12] Moses, G.A., and G.R. Magelssen, "PHD-IV, A Plasma Hydrodynamics-Thermonuclear Burn-Radiative Transfer Computer Code," University of Wisconsin Fusion Engineering Program Report UWFDM-194 (February 1979).

[13] Uesaka, M., and G.A. Moses, "Comparison of Two Temperature and Multi-frequency Group Models of Radiative Transfer - Applied to Microfireball Dynamics in Light Ion Fusion Target Chambers," University of Wisconsin Fusion Engineering Program Report UWFDM-534 (August 1983).

[14] Sweeney, M.A. and D.L. Cook, Bull. Am. Phys. Soc. 24, 1072 (1979); M.A. Sweeney, "Particle Beam Fusion Progress Report, January-June 1980," Sandia National Laboratory, Albuquerque, NM.

[15] Zeldovich, V., and Y. Raizer, *Physics of Shock Waves and High Temperature Hydrodynamic Phenomena*, Vol. I, Academic Press, New York (1966), p. 93.

[16] Reference [14], Vol. 1, p. 63.

[17] Ibid., Vol. 1, p. 154.

APPENDIX A

In this appendix we include plots of all of the hydrodynamics calculations done in this survey.

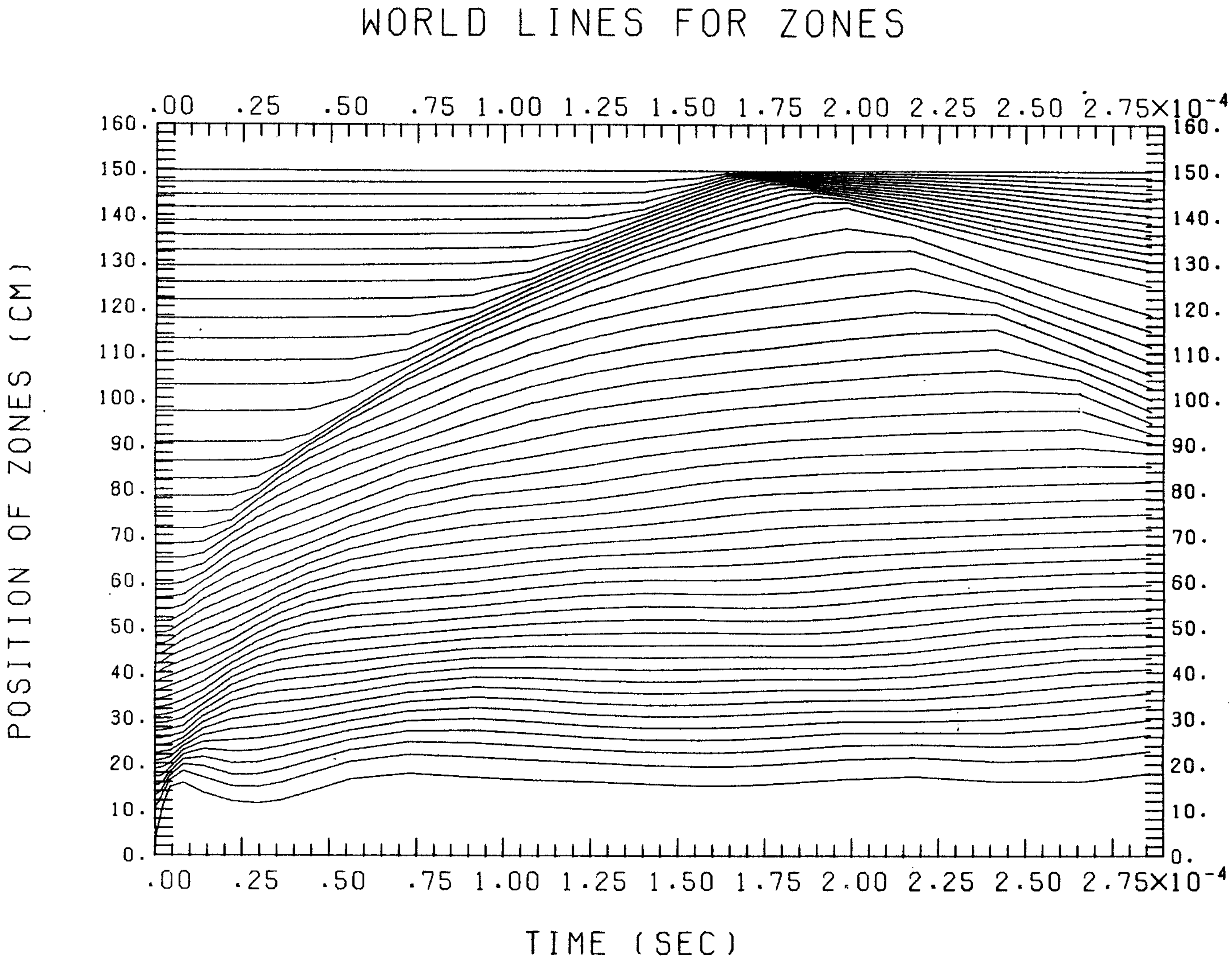

Fig. A.1. R-t plot of Lagrangian zones (50 MJ, 1.5 m).

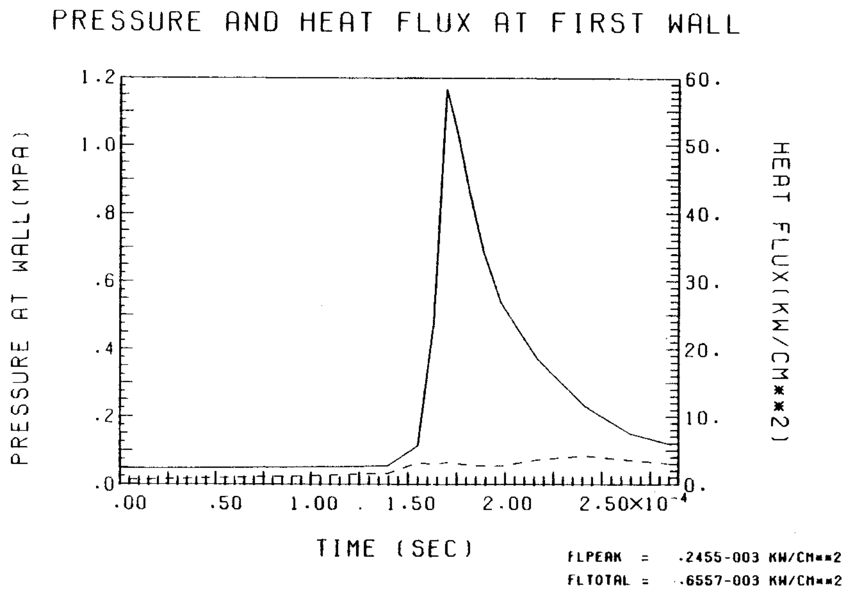

Fig. A.2. Pressure (solid line) and heat flux (dotted line) at the first wall including the first heat pulse (50 MJ, 1.5 m).

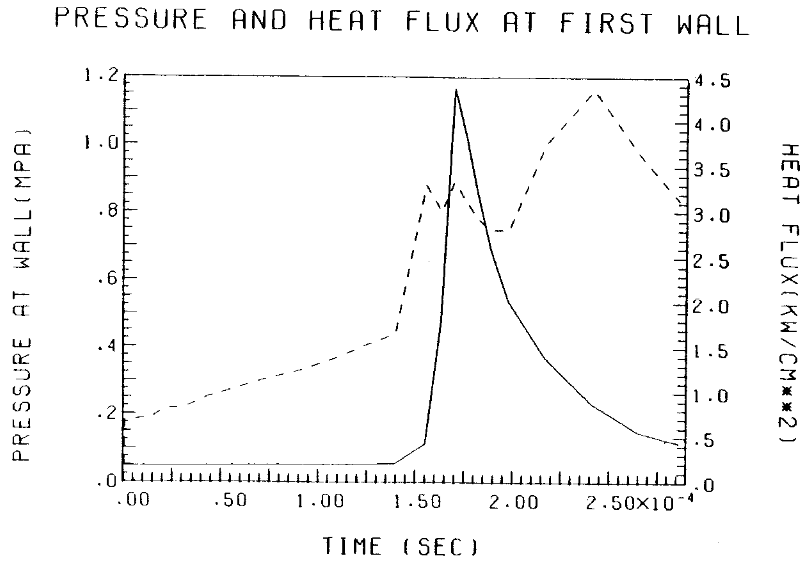

Fig. A.3. Pressure and heat flux (dotted line) at the first wall not including the initial heat pulse. This is just a re-scaled version of A.2 (50 MJ, 1.5 m).

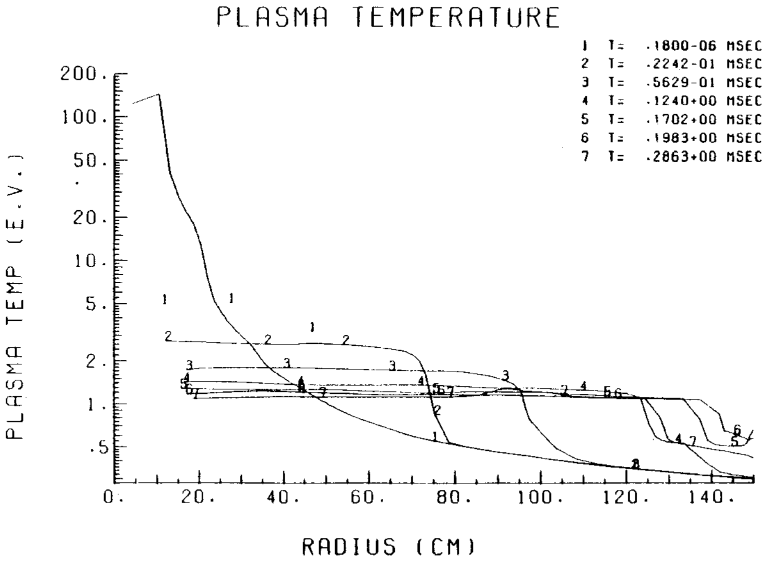

Fig. A.4. Plasma temperature profiles at different times (50 MJ, 1.5 m).

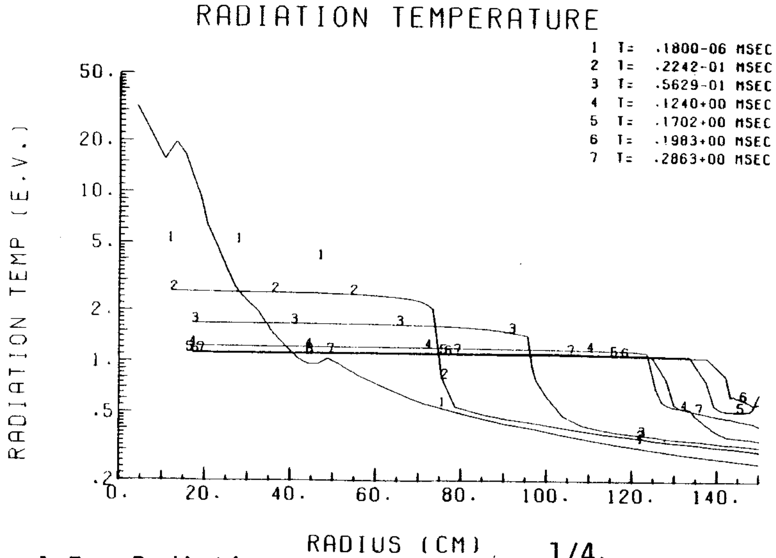

Fig. A.5. Radiation temperature ($\sim E_R^{1/4}$) profiles at different times (50 MJ, 1.5 m).

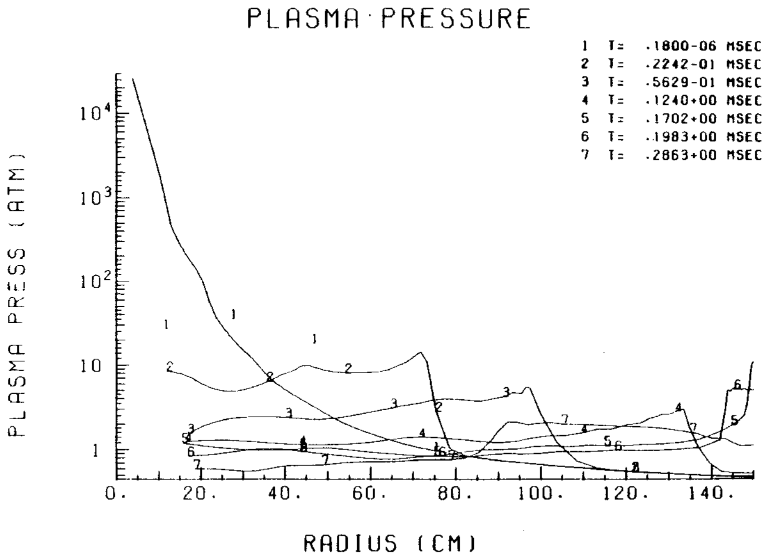

Fig. A.6. Plasma pressure profiles at different times.

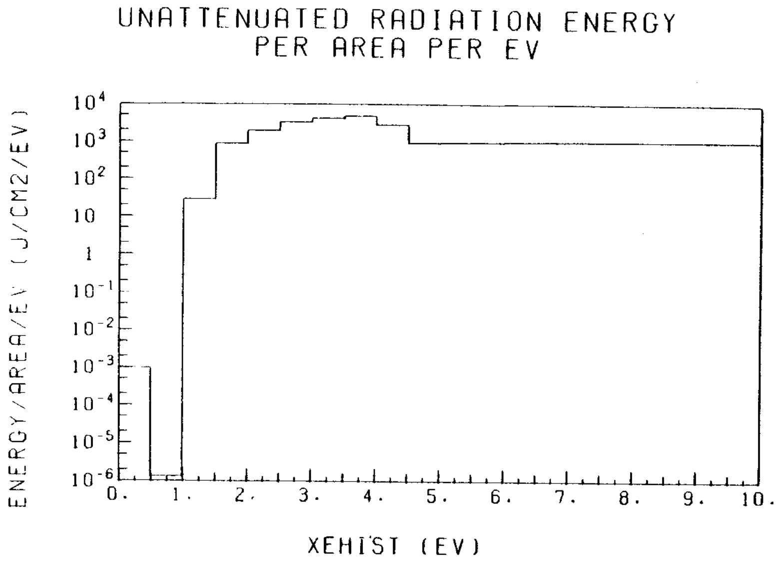

Fig. A.7. Unattenuated target x-ray spectrum at the first wall (50 MJ, 1.5 m).

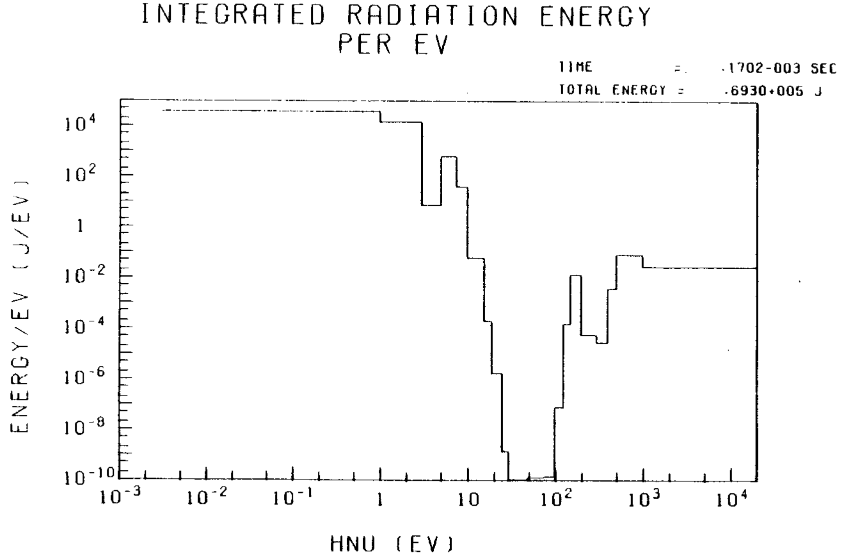

Fig. A.8. Time integrated radiation energy spectrum at the first wall at 0.17 msec (50 MJ, 1.5 m).

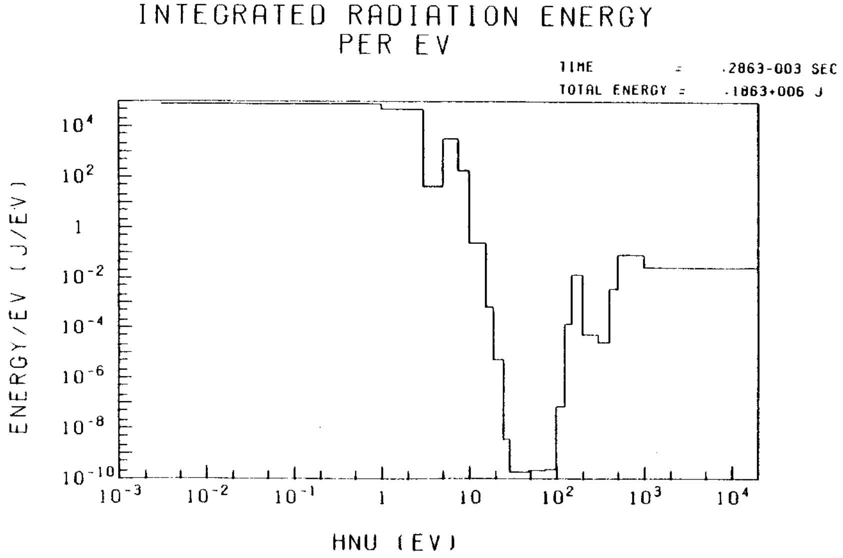

Fig. A.9. Time integrated radiation energy spectrum at the first wall at 0.368 msec (50 MJ, 1.5 m).

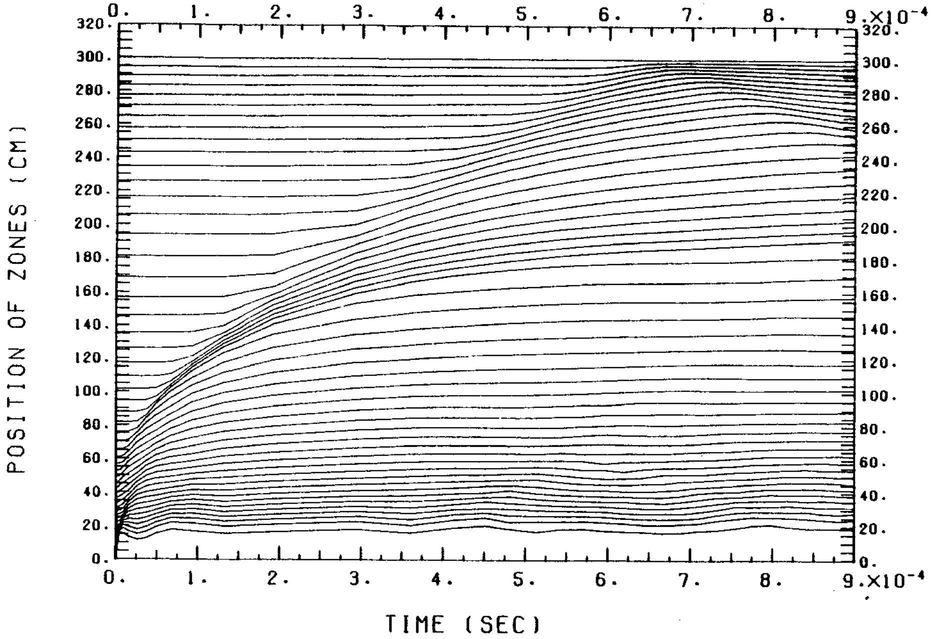

Fig. A.10. R-t plot of Lagrangian zones (50 MJ, 3 m).

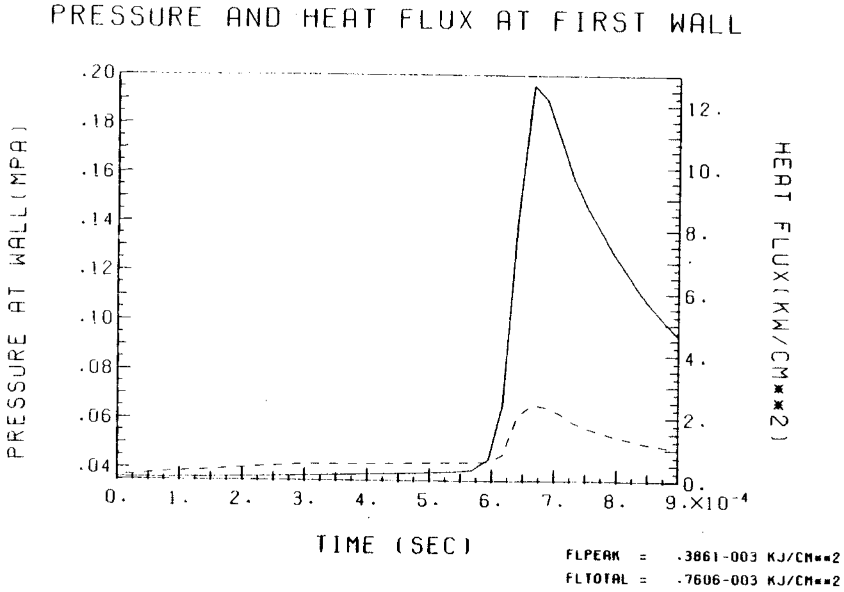

Fig. A.11. Pressure (solid line) and heat flux (dotted line) at the first wall including the first heat pulse (50 MJ, 3 m).

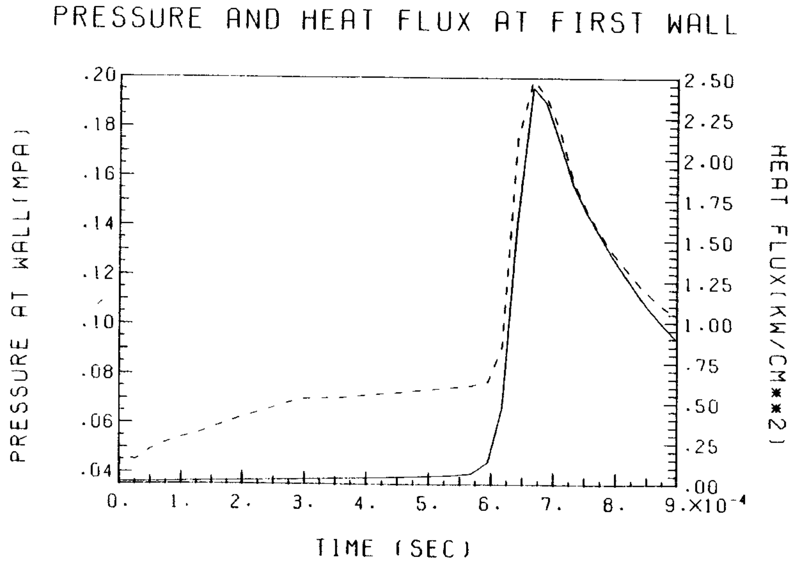

Fig. A.12. Pressure and heat flux at the first wall not including the first heat pulse (50 MJ, 3 m).

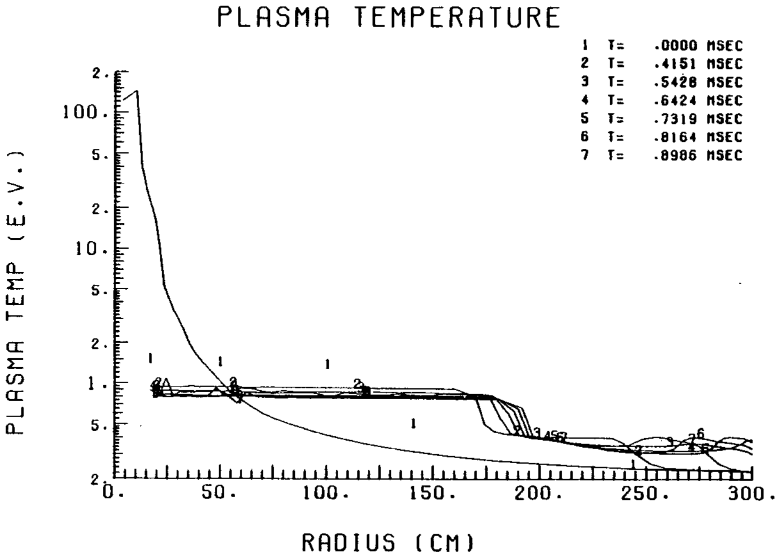

Fig. A.13. Plasma temperature profiles at different times (50 MJ, 3 m).

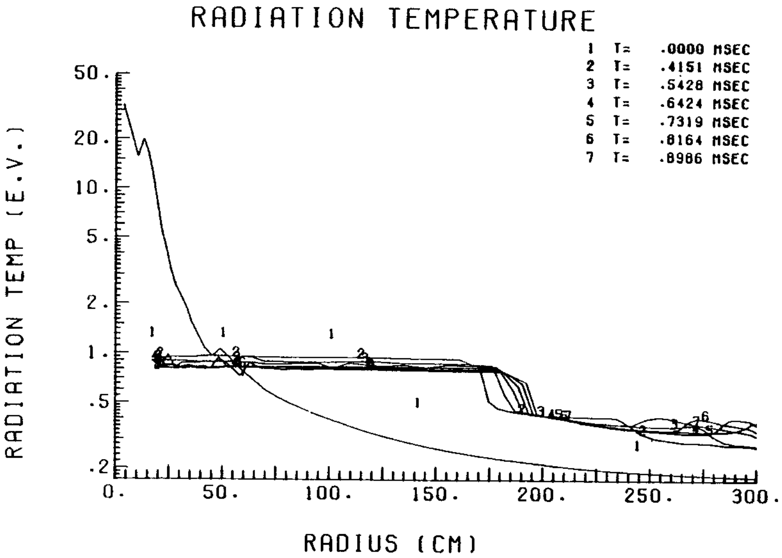

Fig. A.14. Radiation temperature profiles at different times (50 MJ, 3 m).

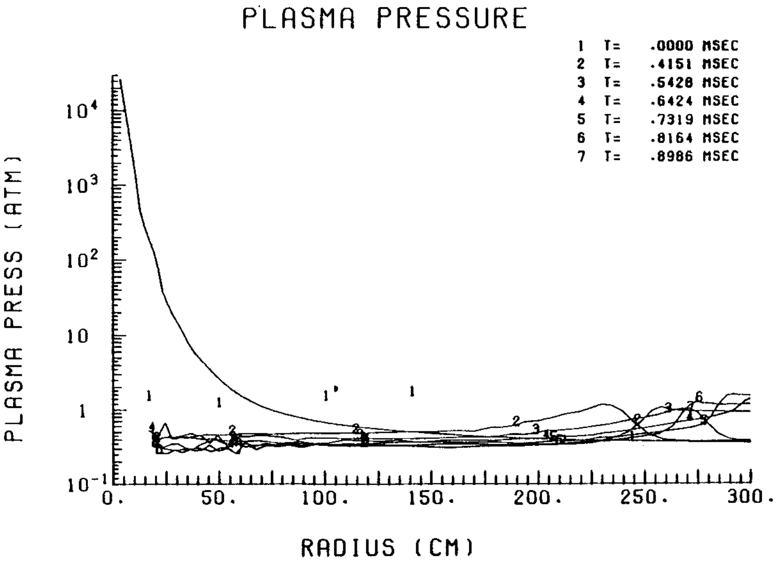

Fig. A.15. Plasma pressure profiles at different times (50 MJ, 3 m).

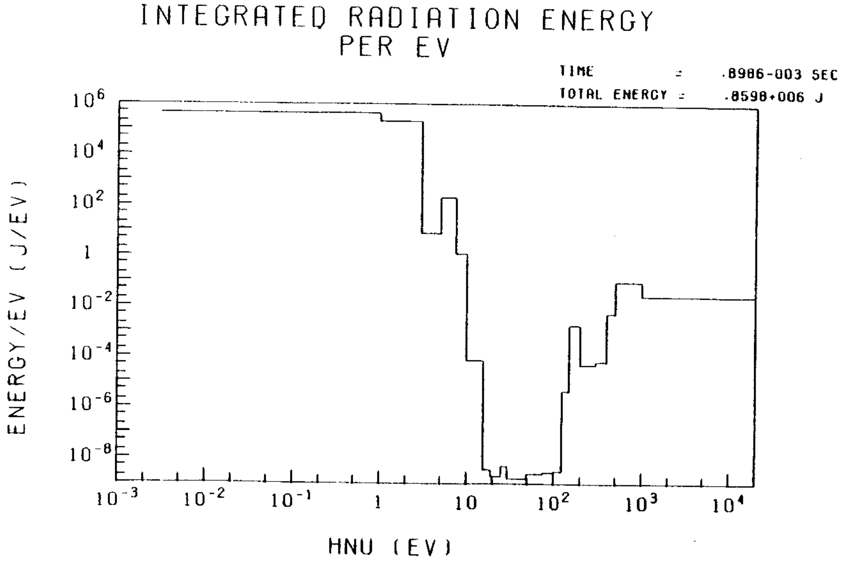

Fig. A.16. Time integrated radiation energy spectrum at the first wall at 0.90 msec (50 MJ, 3 m).

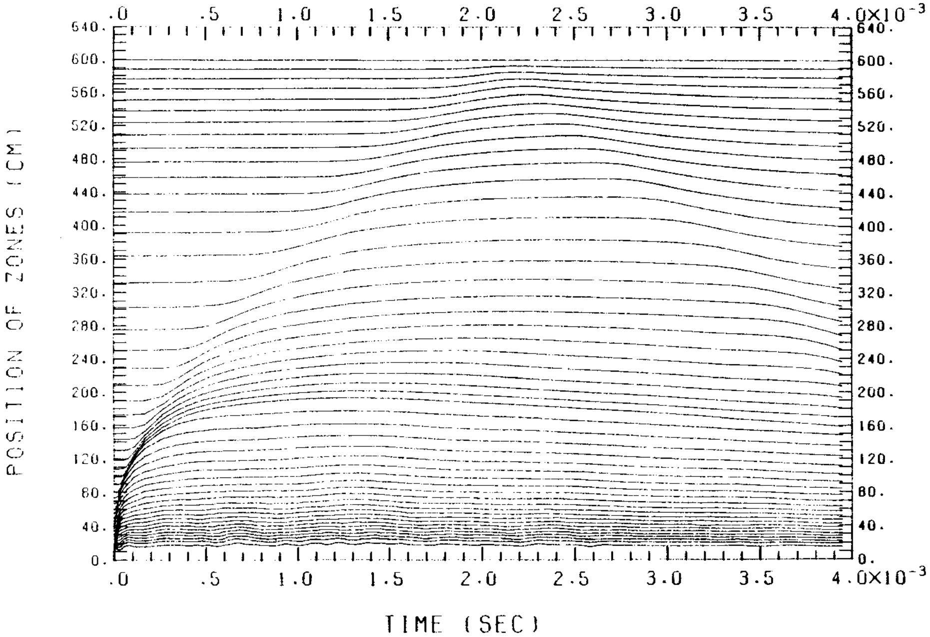

Fig. A.17. R-t plot of Lagrangian zones (50 MJ, 6 m).

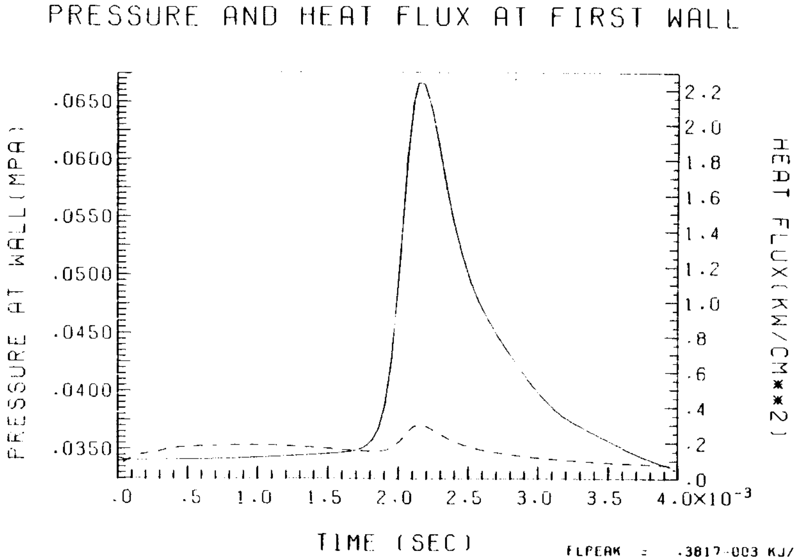

FLPEAK = .3817-003 KJ/CM**2
FLTOTAL = .6280-003 KJ/CM**2

Fig. A.18. Pressure (solid line) and heat flux (dotted line) at the first wall including the first heat pulse (50 MJ, 6 m).

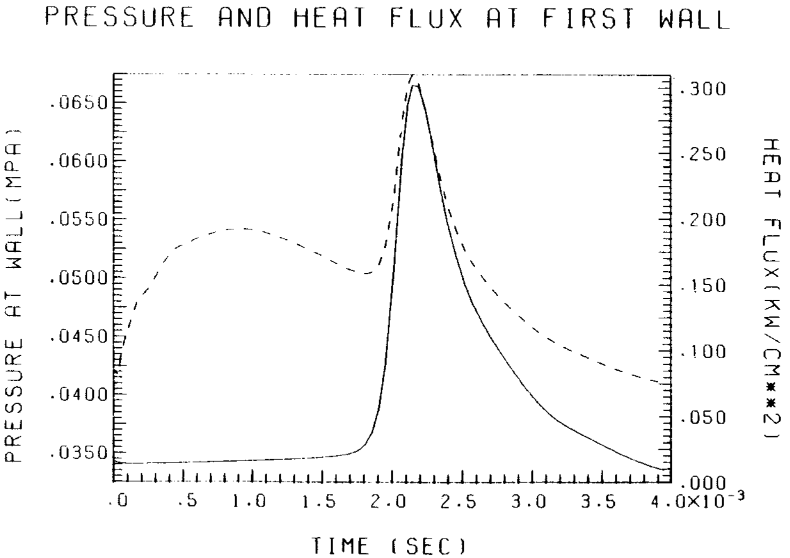

Fig. A.19. Pressure and heat flux at the first wall not including the first heat pulse (50 MJ, 6 m).

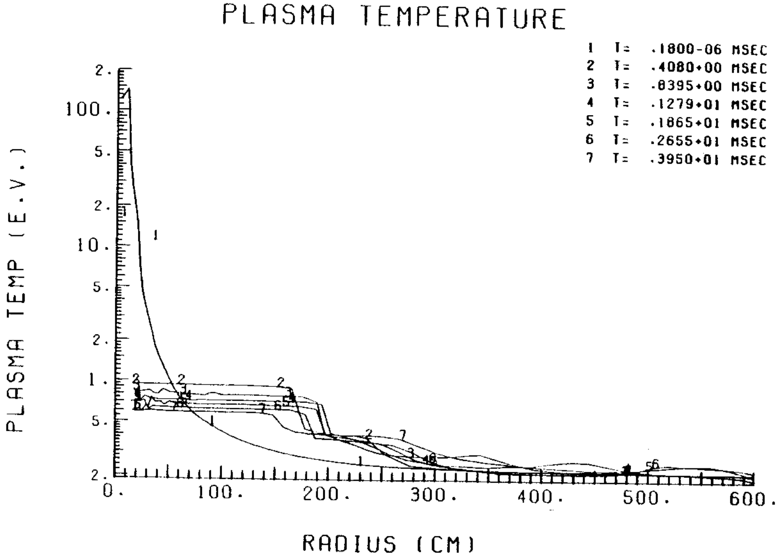

Fig. A.20. Plasma temperature profiles at different times (50 MJ, 6 m).

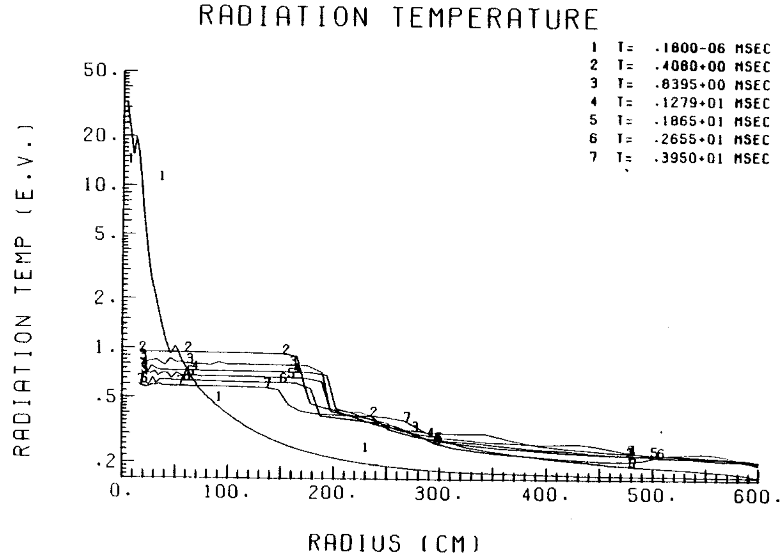

Fig. A.21. Radiation temperature profiles at different times (50 MJ, 6 m).

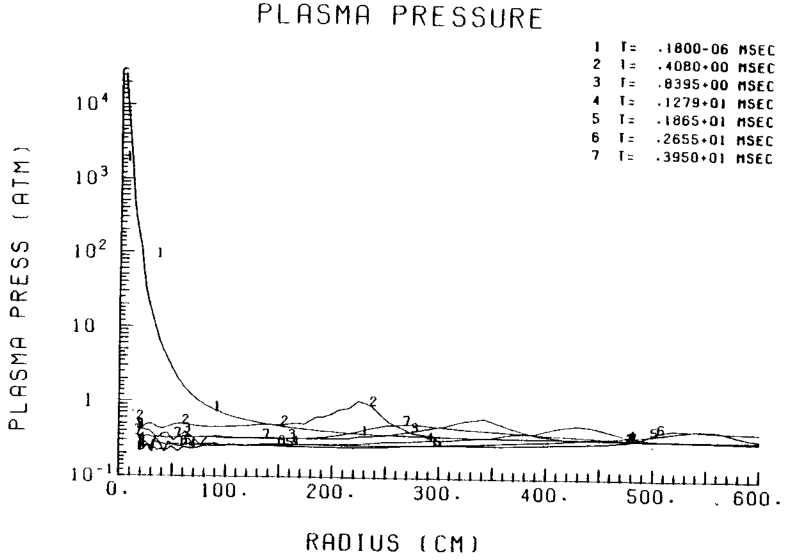

Fig. A.22. Plasma pressure profiles at different times (50 MJ, 6 m).

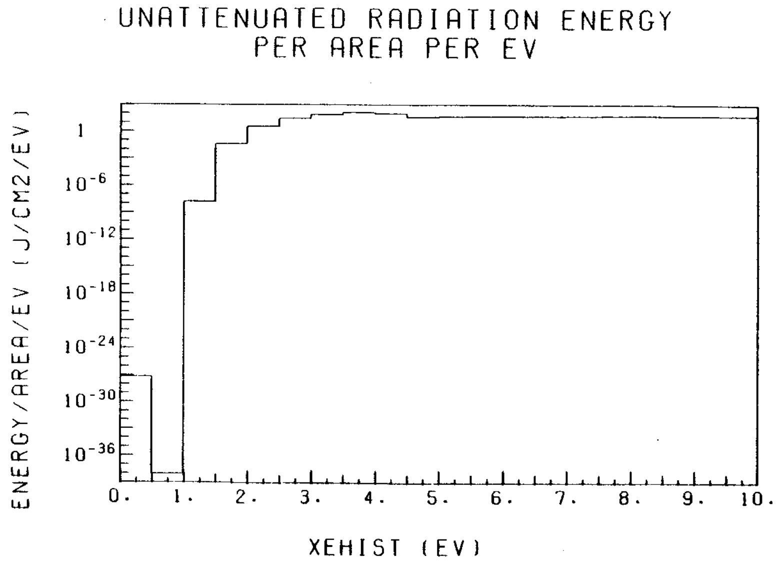

Fig. A.23. Unattenuated target x-ray spectrum at the first wall (50 MJ, 6 m).

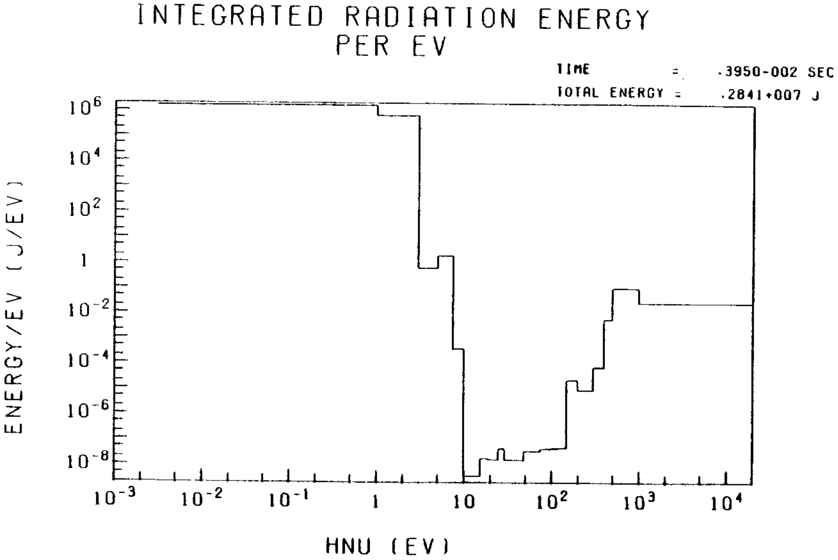

Fig. A.24. Time integrated radiation energy spectrum at the first wall at 3.95 msec (50 MJ, 6 m).

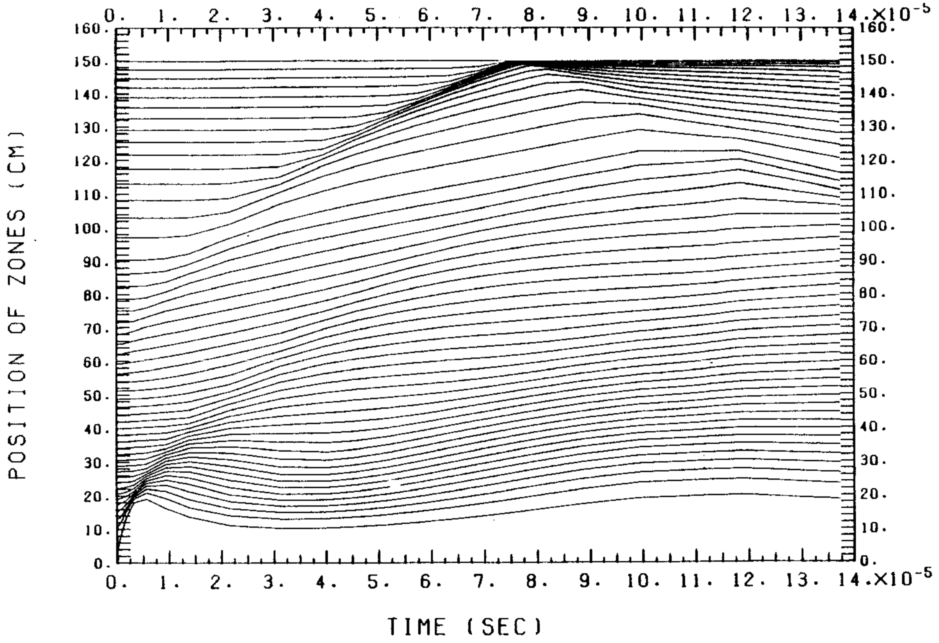

Fig. A.25. R-t plot of Lagrangian zones (200 MJ, 1.5 m).

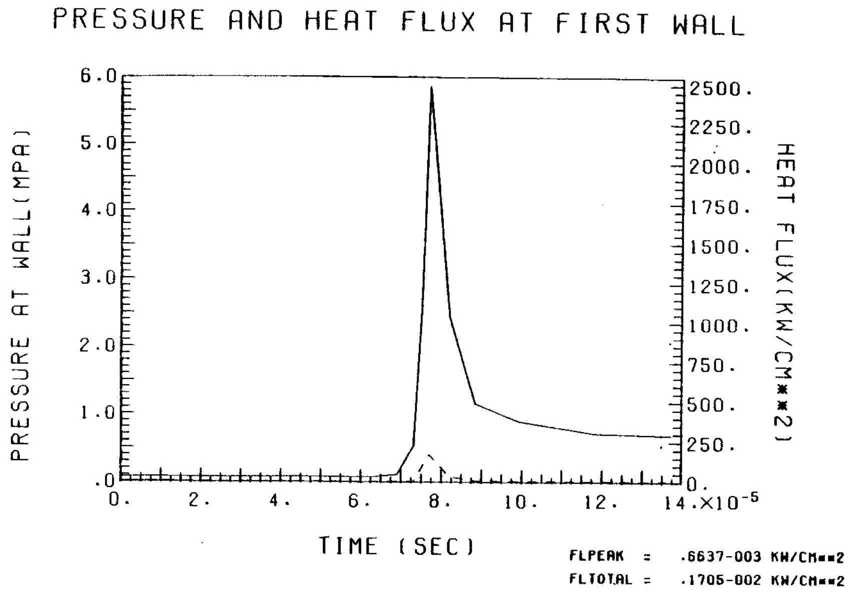

Fig. A.26. Pressure (solid line) and heat flux (dotted line) at the first wall including the first heat pulse (200 MJ, 1.5 m).

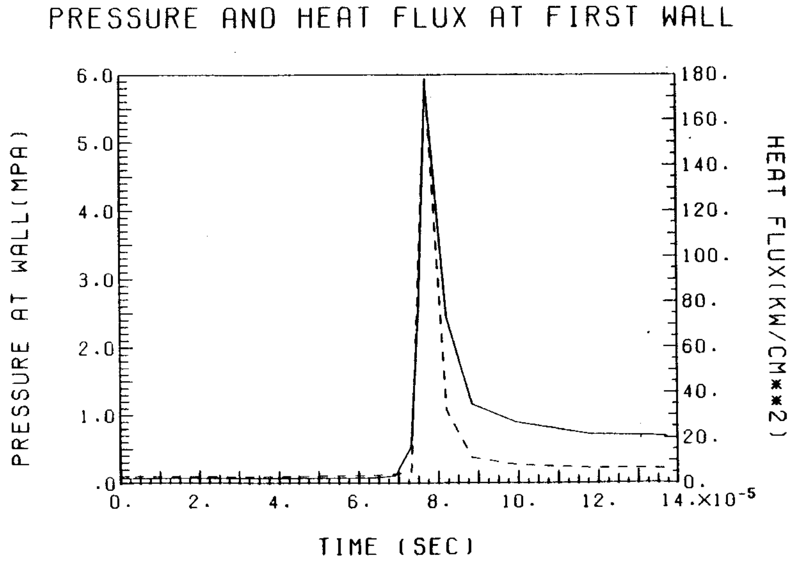

Fig. A.27. Pressure and heat flux at the first wall not including the first heat pulse (200 MJ, 1.5 m).

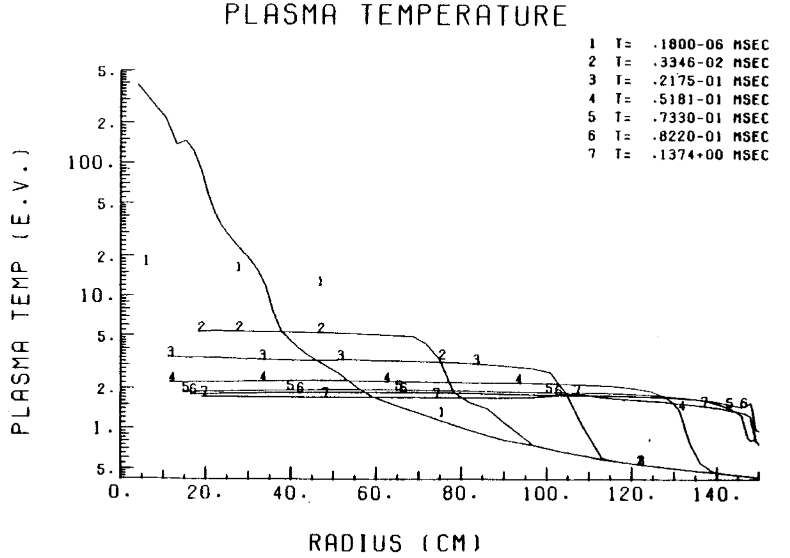

Fig. A.28. Plasma temperature profiles at different times (200 MJ, 1.5 m).

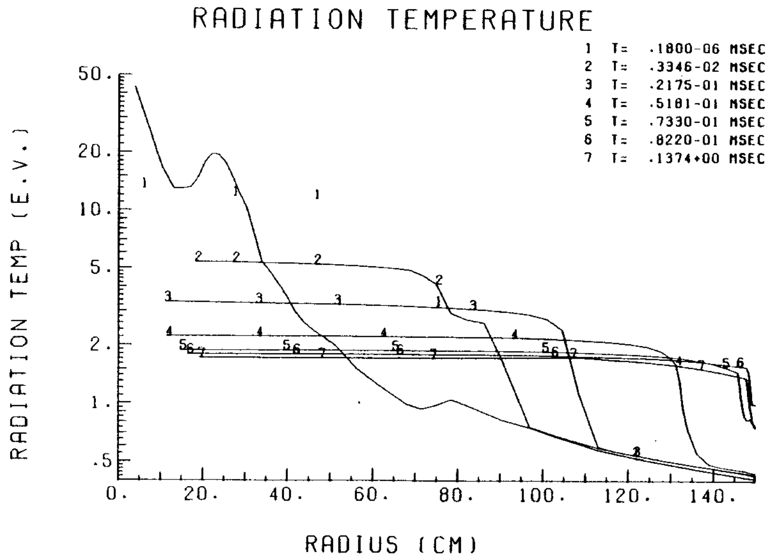

Fig. A.29. Radiation temperature profiles at different times (200 MJ, 1.5 m).

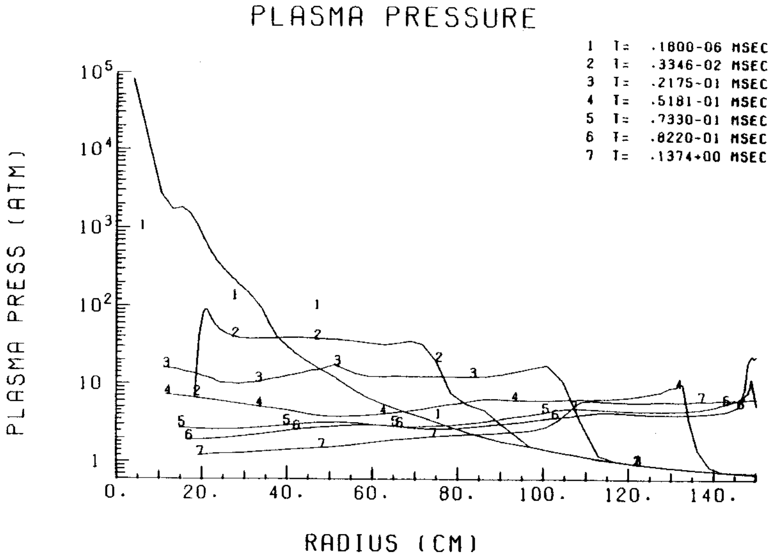

Fig. A.30. Plasma pressure profiles at different times (200 MJ, 1.5 m).

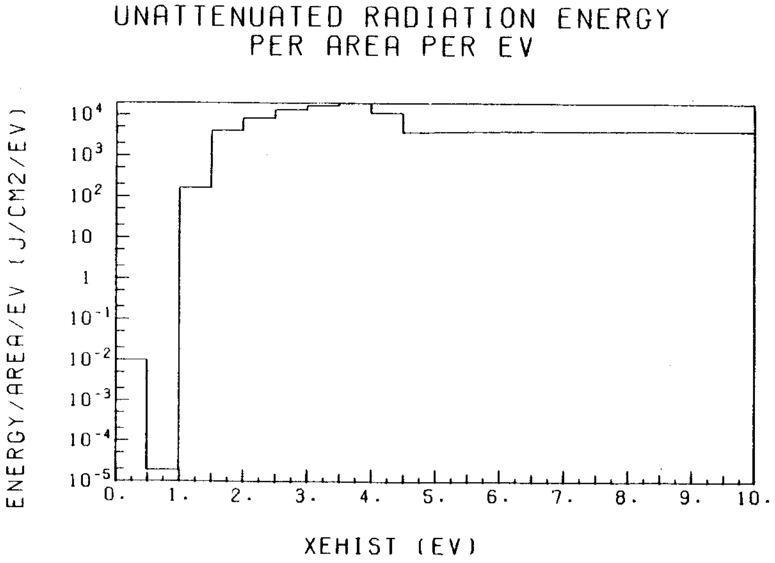

Fig. A.31. Unattenuated target x-ray spectrum at the first wall (200 MJ, 1.5 m).

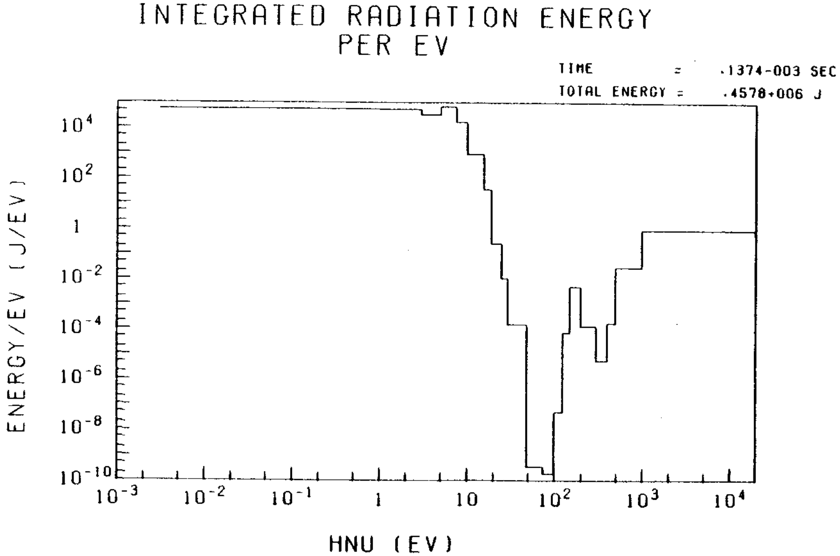

Fig. A.32. Time integrated radiation energy spectrum at the first wall at 0.14 msec (200 MJ, 1.5 m).

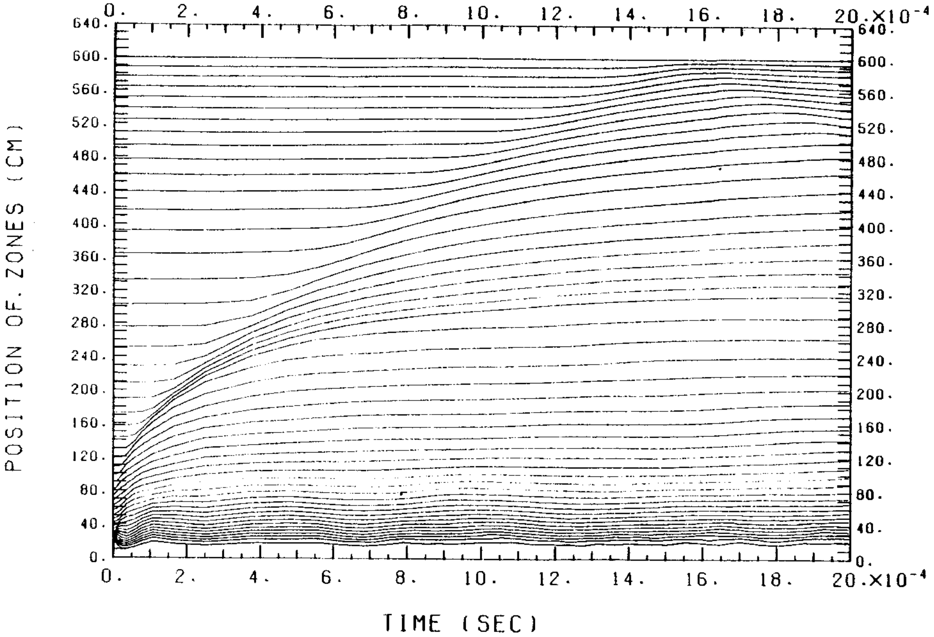

Fig. A.33. R-t plot of Lagrangian zones (200 MJ, 6 m).

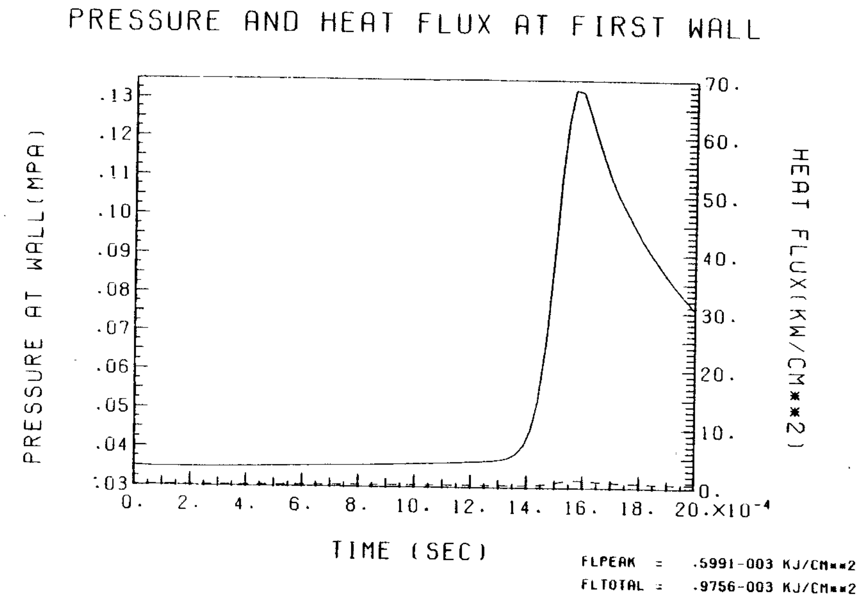

Fig. A.34. Pressure (solid line) and heat flux (dotted line) at the first wall including the first heat pulse (200 MJ, 6 m).

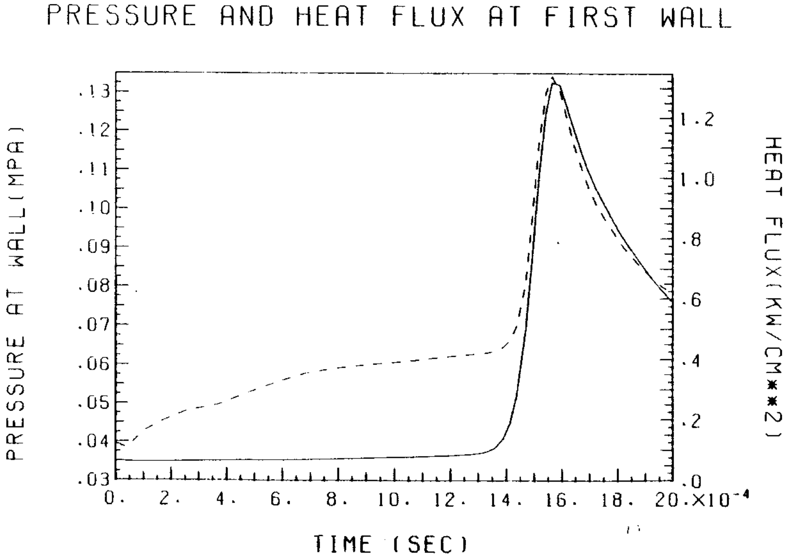

Fig. A.35. Pressure and heat flux at the first wall not including the first heat pulse (200 MJ, 6 m).

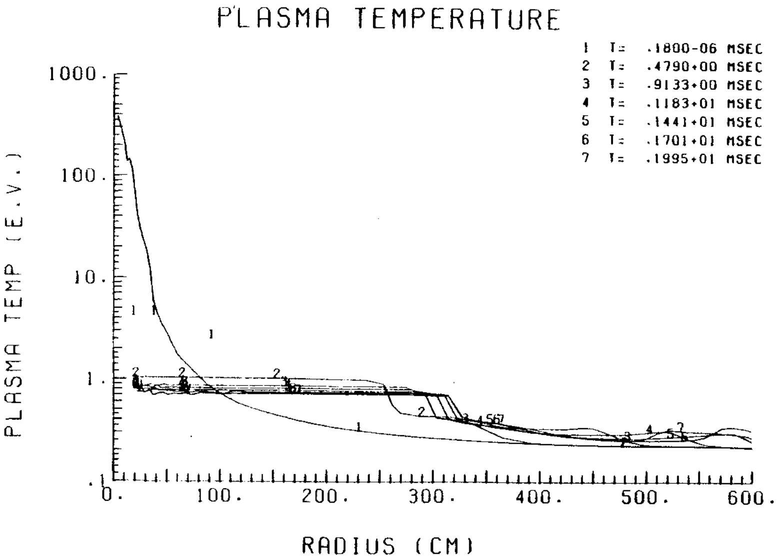

Fig. A.36. Plasma temperature profiles at different times (200 MJ, 6 m).

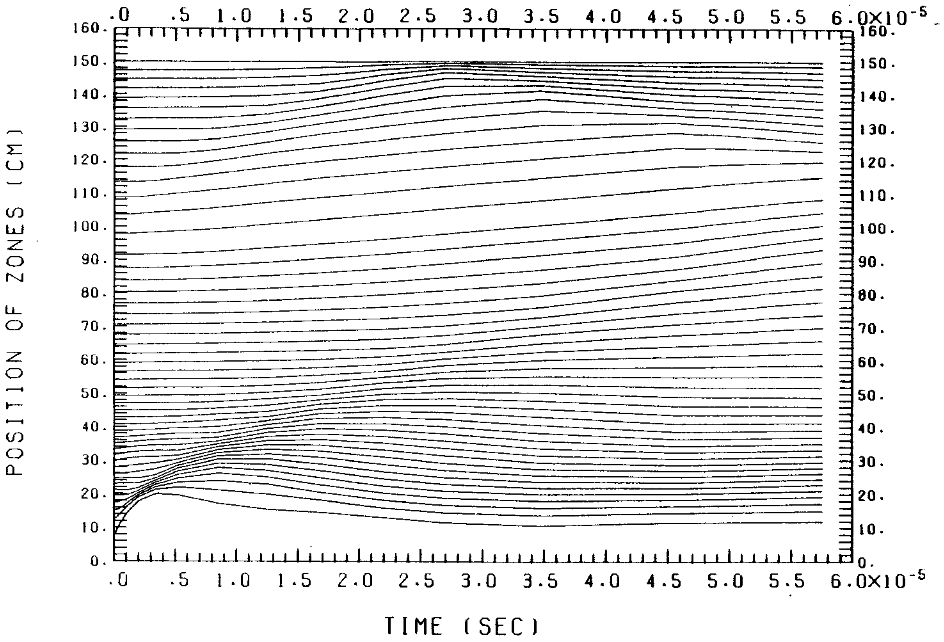

Fig. A.41. R-t plot of Lagrangian zones (800 MJ, 1.5 m).

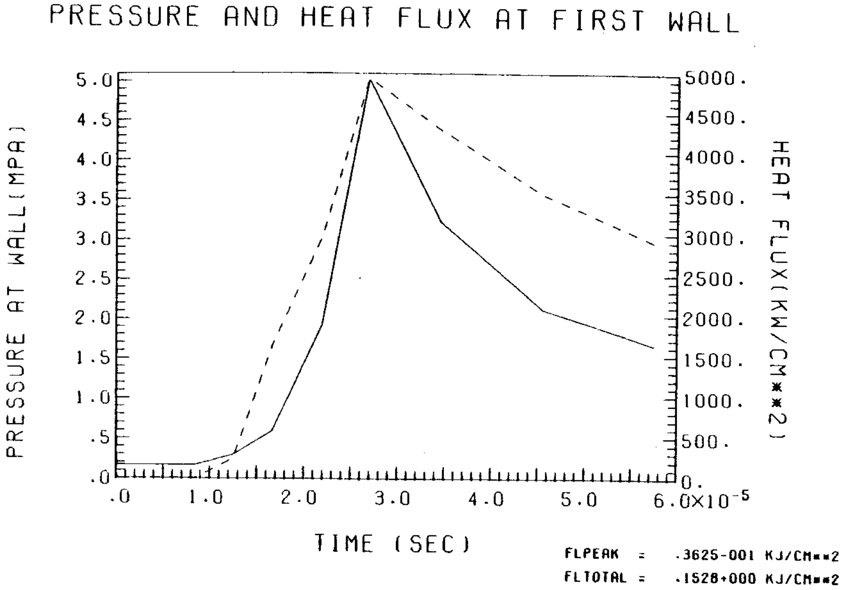

Fig. A.42. Pressure (solid line) and heat flux (dotted line) at the first wall (800 MJ, 1.5 m).

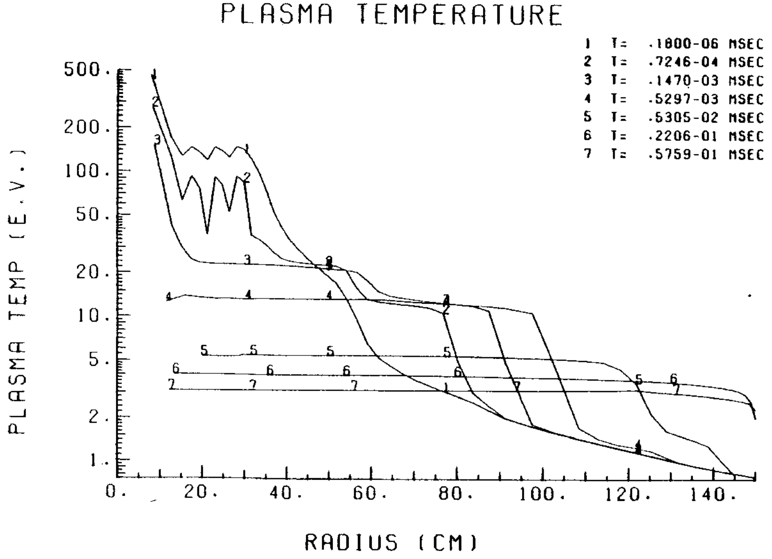

Fig. A.43. Plasma temperature profiles at different times (800 MJ, 1.5 m).

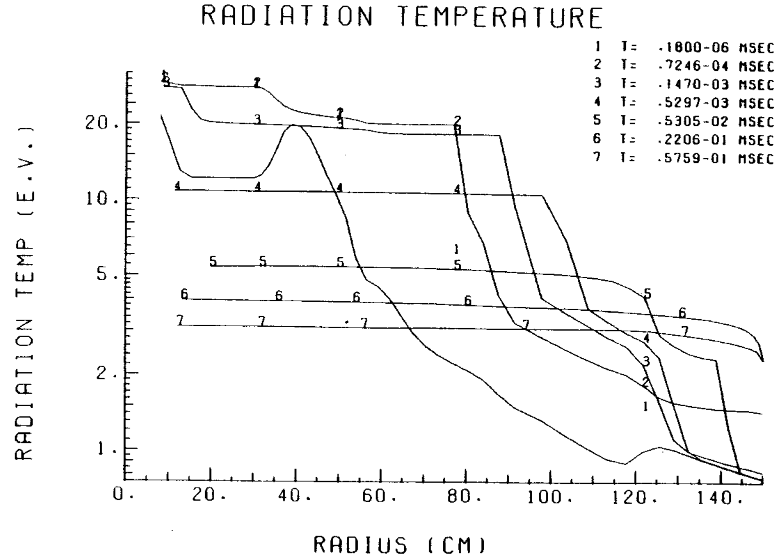

Fig. A.44. Radiation temperature profiles at different times (800 MJ, 1.5 m).

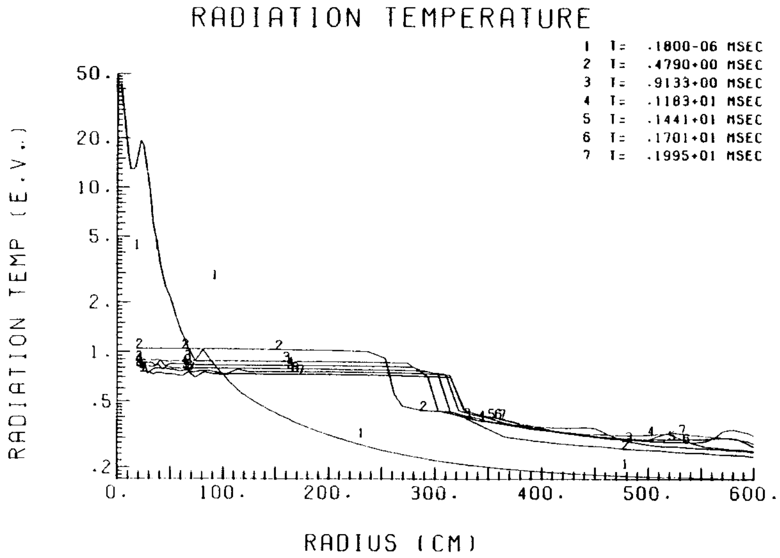

Fig. A.37. Radiation temperature profiles at different times (200 MJ, 6 m).

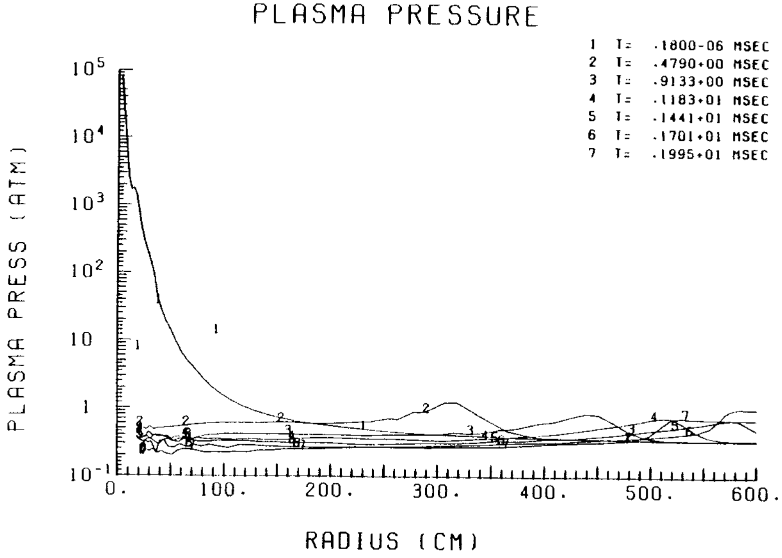

Fig. A.38. Plasma pressure profiles at different times (200 MJ, 6 m).

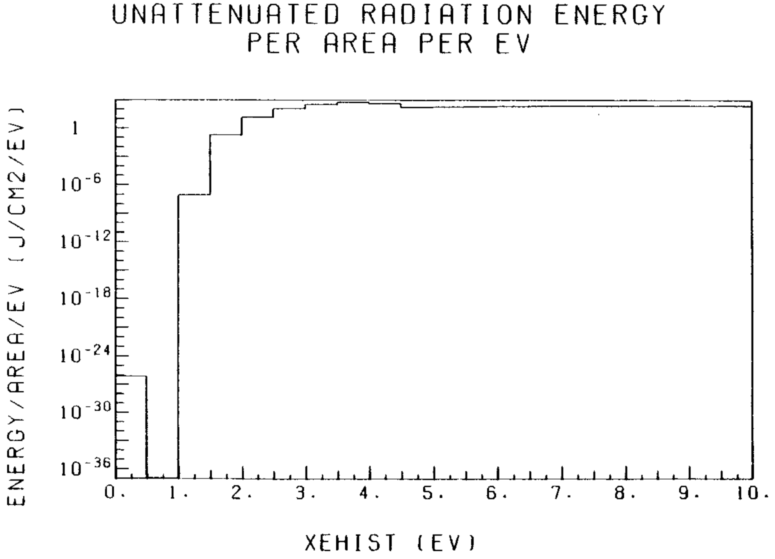

Fig. A.39. Unattenuated target x-ray spectrum at the first wall (200 MJ, 6 m).

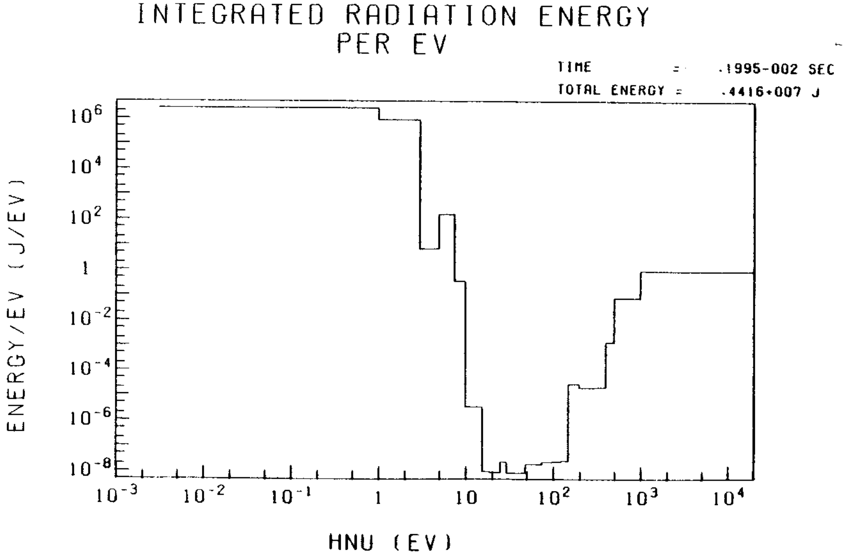

Fig. A.40. Time integrated radiation energy spectrum at the first wall at 2 msec (200 MJ, 6 m).

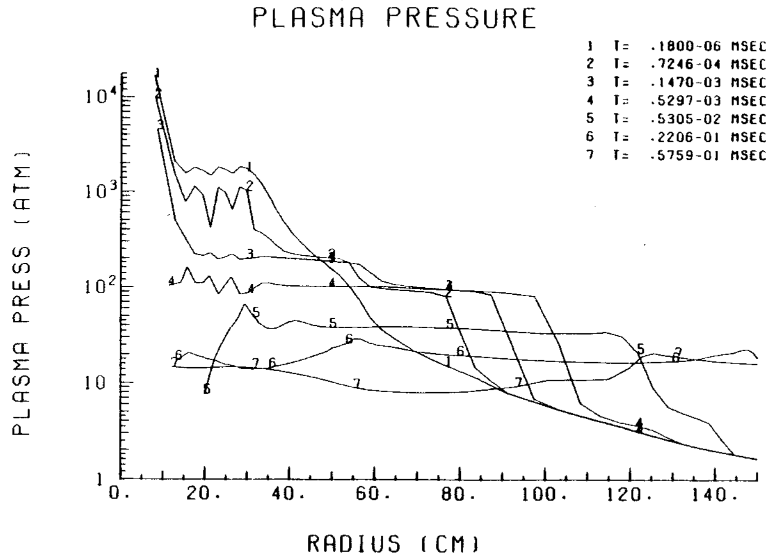

Fig. A.45. Plasma pressure profiles at different times (800 MJ, 1.5 m).

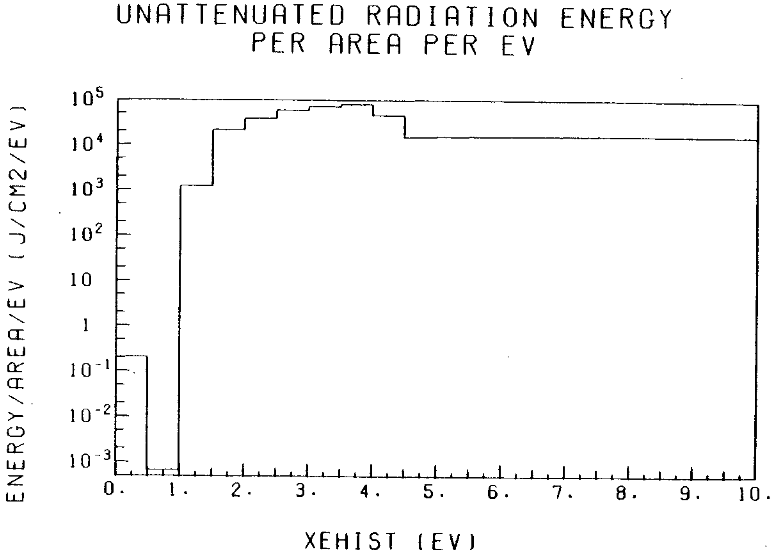

Fig. A.46. Unattenuated target x-ray spectrum at the first wall (800 MJ, 1.5 m).

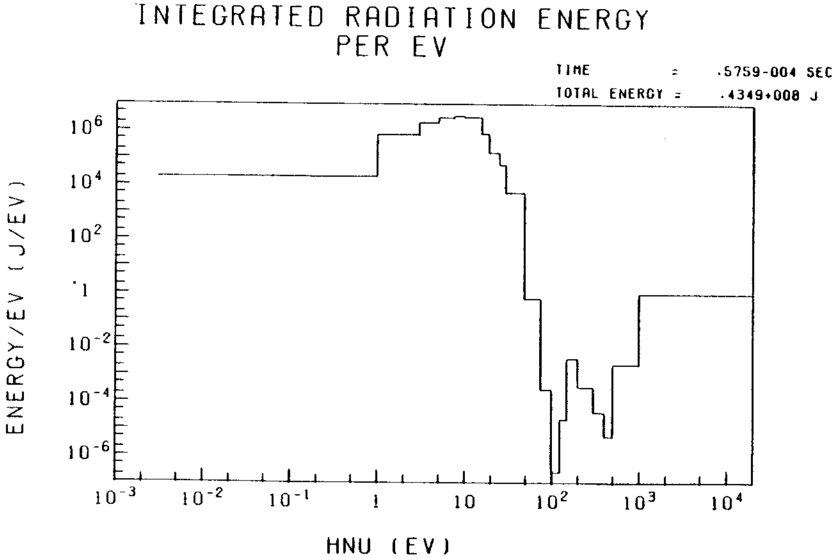

Fig. A.47. Time integrated radiation energy spectrum at the first wall at 0.57 msec (800 MJ, 1.5 m).

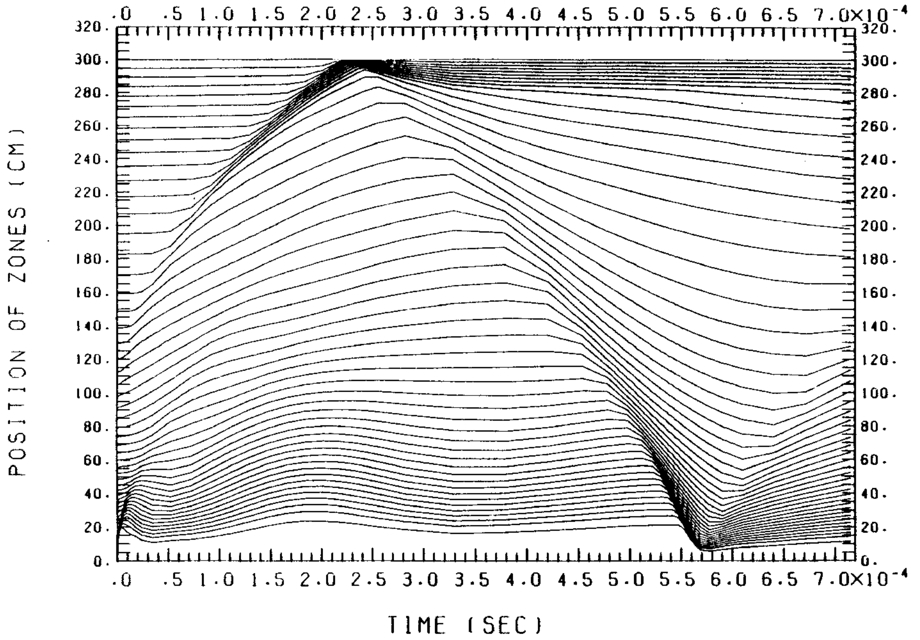

Fig. A.48. R-t plot of Lagrangian zones (800 MJ, 3 m).

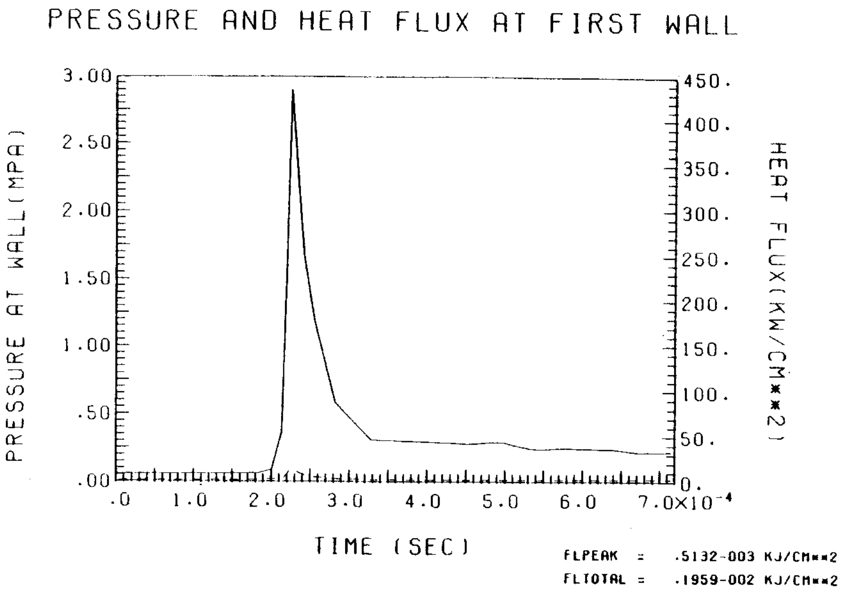

Fig. A.49. Pressure (solid line) and heat flux (dotted line) at the first wall including the first heat pulse (800 MJ, 3 m).

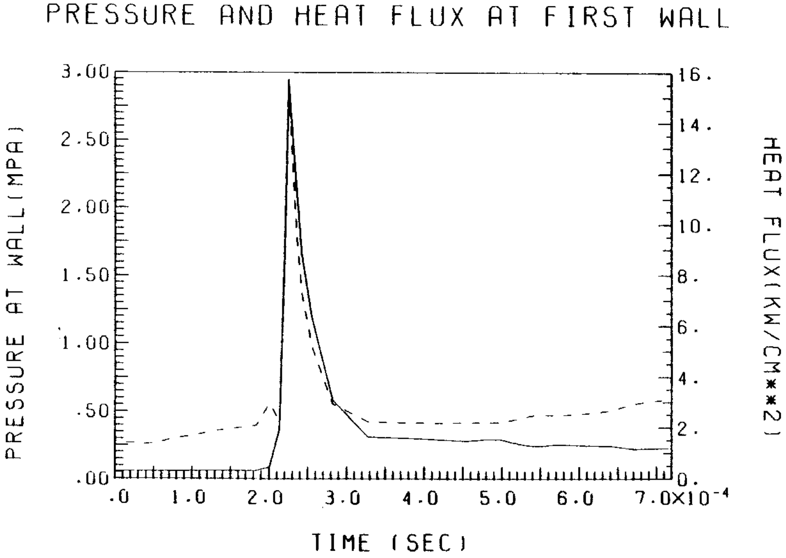

Fig. A.50. Pressure and heat flux at the first wall not including the first heat pulse (800 MJ, 3 m).

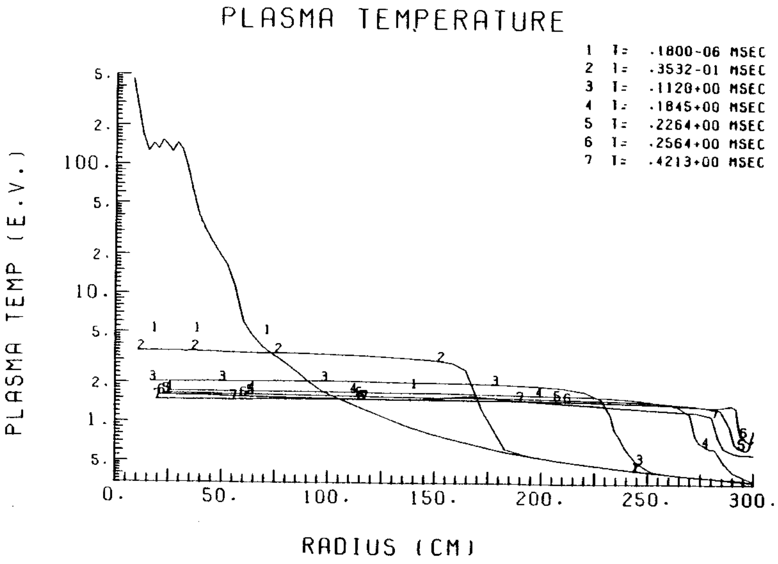

Fig. A.51. Plasma temperature profiles at different times (800 MJ, 3 m).

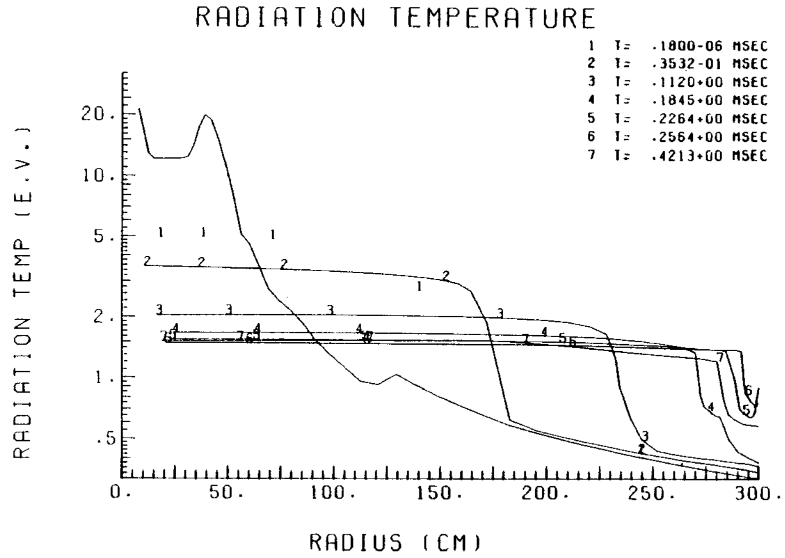

Fig. A.52. Radiation temperature profiles at different times (800 MJ, 3 m).

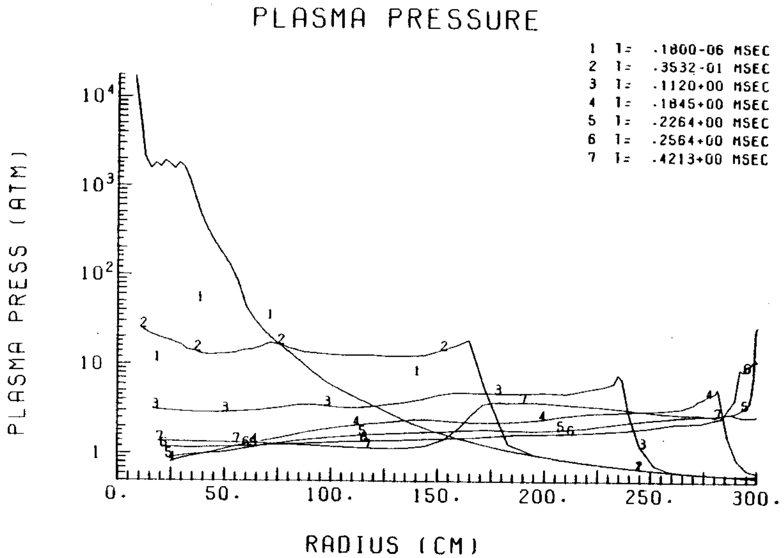

Fig. A.53. Plasma pressure profiles at different times (800 MJ, 3 m).

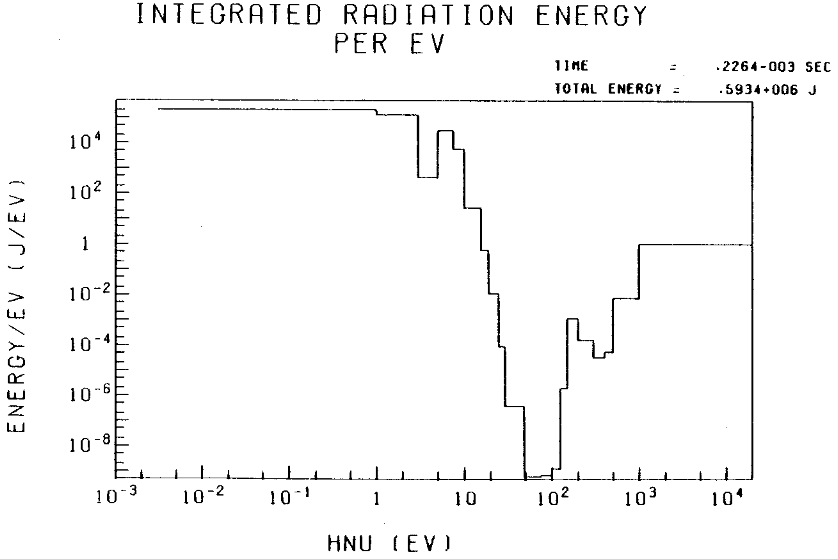

Fig. A.54. Time integrated radiation energy spectrum at the first wall at 0.23 msec (800 MJ, 3 m).

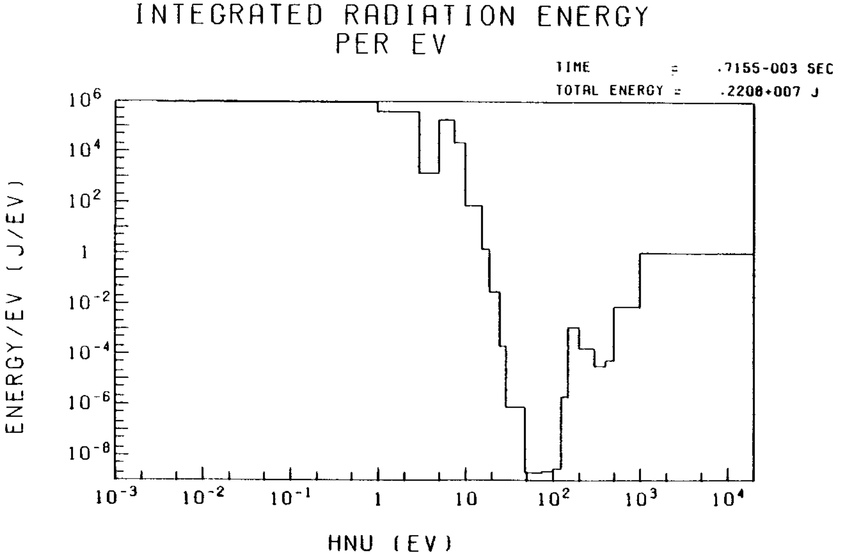

Fig. A.55. Time integrated radiation energy spectrum at the first wall at 0.71 msec (800 MJ, 3 m).

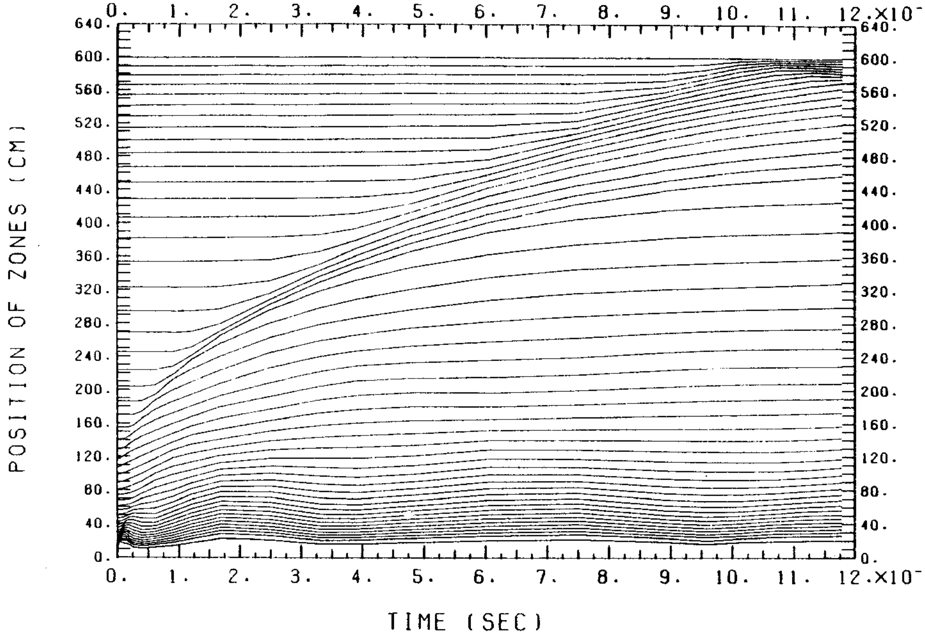

Fig. A.56. R-t plot of Lagrangian zones (800 MJ, 6 m).

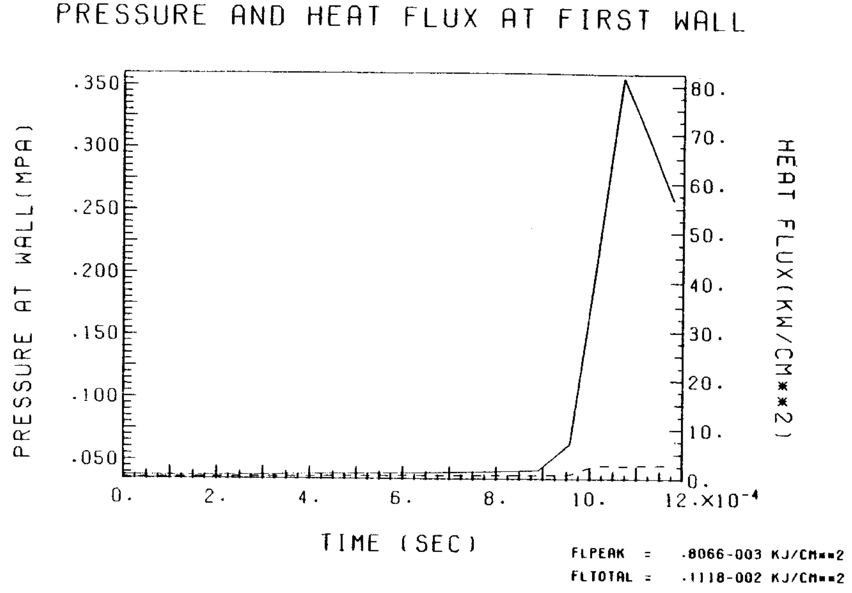

Fig. A.57. Pressure (solid line) and heat flux (dotted line) at the first wall including the first heat pulse (800 MJ, 6 m).

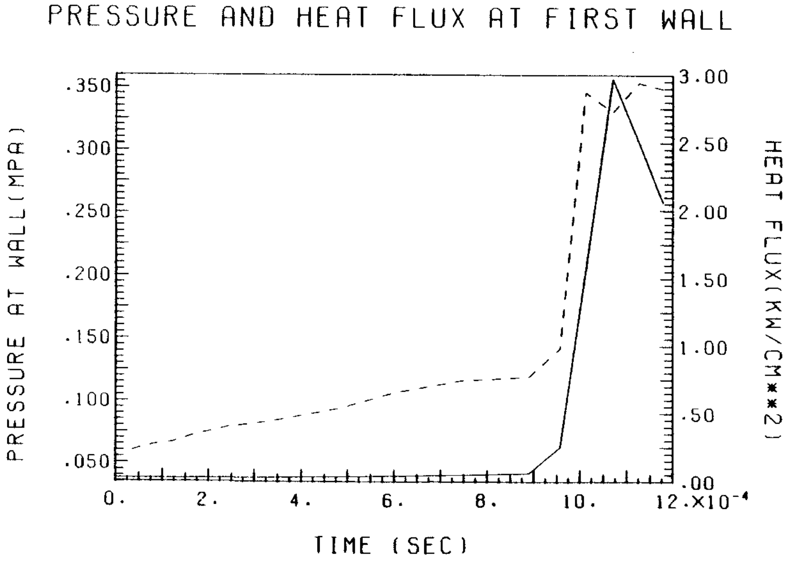

Fig. A.58. Pressure and heat flux at the first wall not including the first heat pulse (800 MJ, 6 m).

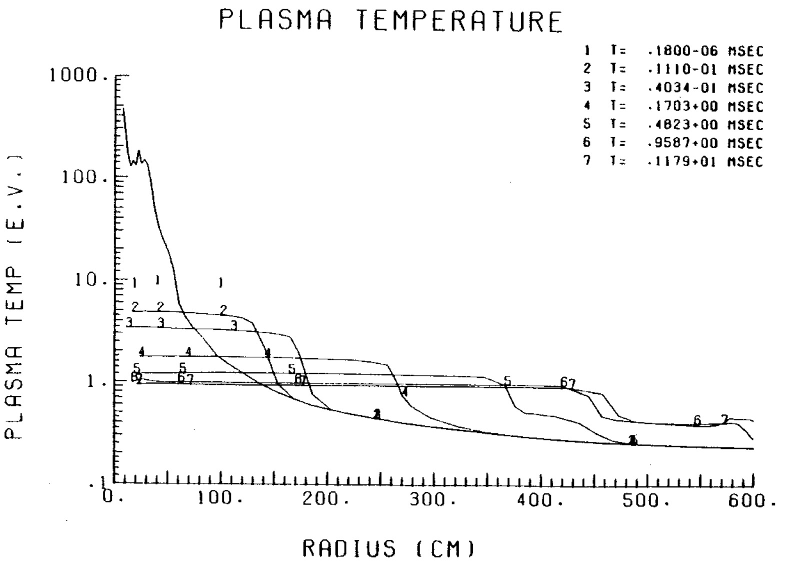

Fig. A.59. Plasma temperature profiles at different times (800 MJ, 6 m).

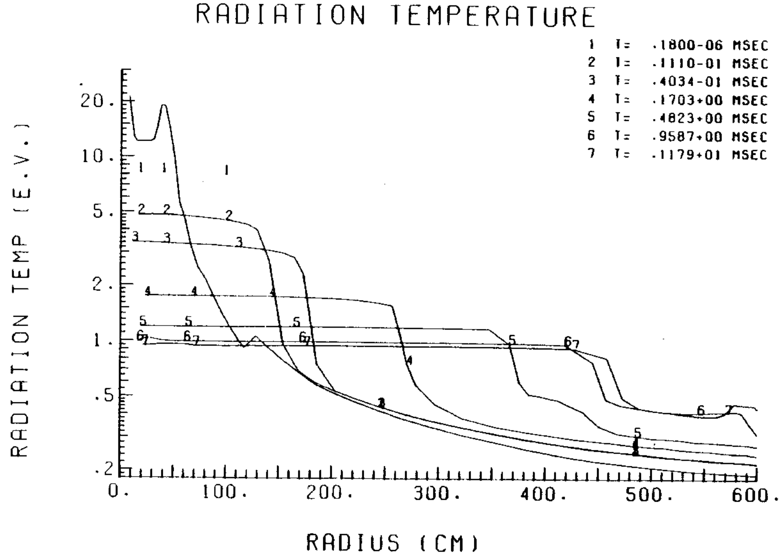

Fig. A.60. Radiation temperature profiles at different times (800 MJ, 6 m).

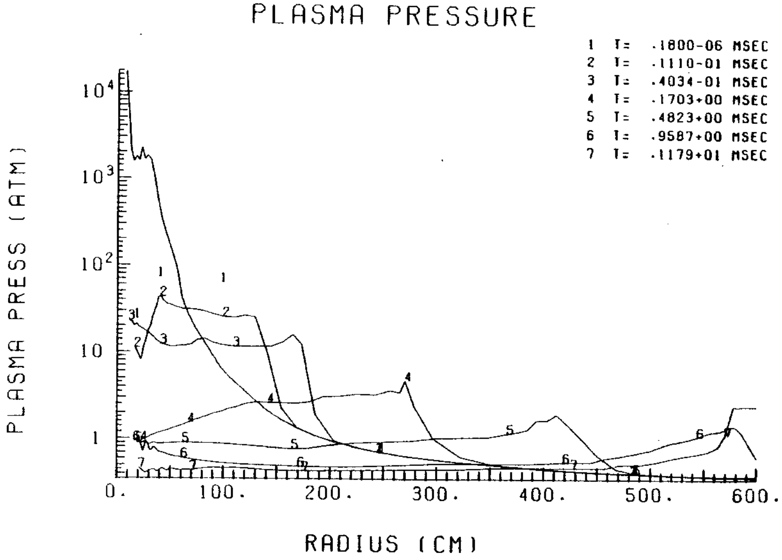

Fig. A.61. Plasma pressure profiles at different times (800 MJ, 6 m).

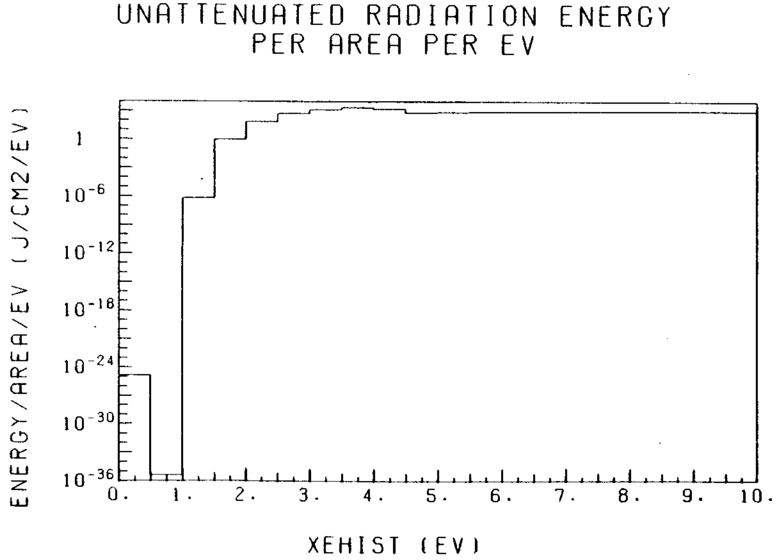

Fig. A.62. Unattenuated target x-ray spectrum at the first wall (800 MJ, 6 m).

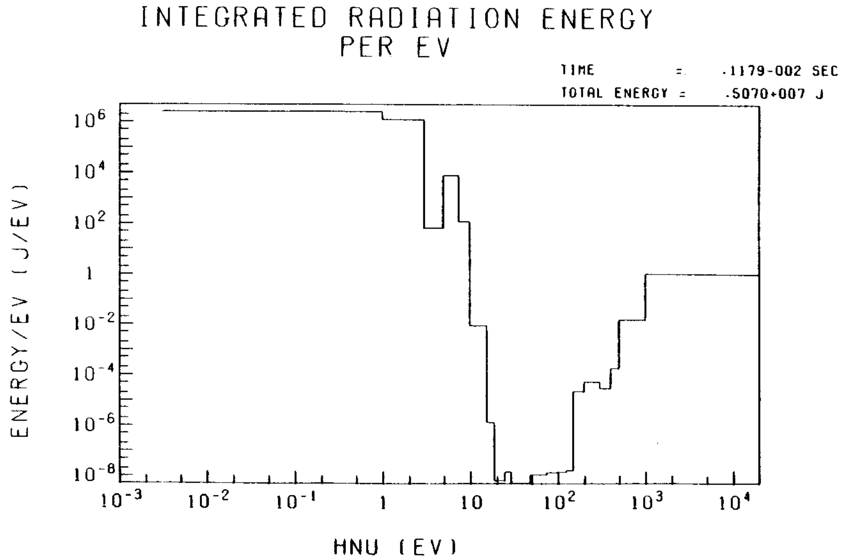

Fig. A.63. Time integrated radiation energy spectrum at the first wall at 1.18 msec (800 MJ, 6 m).